IEEE Access
Multidisciplinary | Rapid Review | Open Access Journal

Received March 12, 2021, accepted March 23, 2021, date of publication March 29, 2021, date of current version April 9, 2021.

Digital Object Identifier 10.1109/ACCESS.2021.3069454

Online Short-Circuit Protection Strategy of an Electric Powerpack for Electric Oil Pump Applications

YOUNGWOO NOH, (Graduate Student Member, IEEE), WONKYU KIM, AND JU LEE, (Senior Member, IEEE)
Department of Electrical Engineering, Hanyang University, Seoul 04763, South Korea
Corresponding author: Ju Lee (julee@hanyang.ac.kr)

ABSTRACT With the trend towards the miniaturisation and electrification of automotive components, the electric oil pump (EOP) is generally designed as an integrated powerpack in which a motor and an electronic control unit (ECU) are combined into an integrated system, with the electronic components of the ECU exposed to harsher temperature environments. The critical weakness of the traditional design is short-circuit failures, and the most common protection method is V_{ds} monitoring. However, this method cannot predict the accurate protection current, indicating that the fault detection level and short-circuit current (SCC) may change depending on the operating temperature and load condition to which the devices are subject. In this case, switching devices can be destroyed or deteriorated if they are unexpectedly placed outside of the protection range. This study proposes an online short-circuit protection method in which the optimal fault threshold can be controlled in real time, in accordance with changes in temperature and load conditions. To this end, this study investigates the cause of fluctuations in SCC and analyses the protection range and qualification time for SCC through worst-case analysis. To determine the optimal fault threshold, the SCC waveform is estimated through circuit analysis and a method of estimating $R_{dson}(T_j)$, which is the cause of SCC fluctuation, is proposed based on simulation and experimental data. Finally, according to $R_{dson}(T_j)$, optimal thresholds are derived and the proposed methods are experimentally-verified. It is found that the SCC could be predicted and managed within the protection range by the proposed new protection method.

INDEX TERMS Automotive electric powerpack, diagnosis, electric oil pump, gate drive circuit, junction temperature, optimal fault threshold, short-circuit protection, short-circuit current waveform.

I. INTRODUCTION

To improve vehicular fuel efficiency, research on the electrification of powertrain components is being actively conducted. A particular focus of these efforts is the electric oil pump (EOP), which is located in the automatic transmission (AT). It provides the pressure and flow required by the system and superseded mechanical oil pumps [1]–[6]. When an AT vehicle enters and releases the idle, stop and go modes, it supplies automatic transmission fluid (ATF) oil to the transmission in order to reduce shift shock, improve efficiency and reduce exhaust gas. Due to transmission space limitations, the EOP has recently often been designed as a powerpack-type unit, with the hydraulic pump of the electric motor and electronic control unit (ECU) integrated [7], [8]. An EOP powerpack consists of mechanical and electrical components, and demand for the reliability and robustness of the electrical components has progressively increased. In particular, the design of diagnostic mechanisms for detecting and reacting to electrical failures should be prioritised.

The most critical electrical failure in an EOP powerpack, is a short-circuit (SC). If the oil circulated to the pump and motor leaks and flows into the ECU, the metallic particles contained in the oil may cause SCs between the pins of the electronic components or printed circuit board (PCB) patterns. Outside of the powerpack, there is a risk that long cables or wire harnesses connecting the battery or transmission control unit could cause SC failures. When a short-circuit-to-battery (SCB) or short-circuit-to-ground (SCG) event occurs in one of the inverter legs, it becomes

The associate editor coordinating the review of this manuscript and approving it for publication was Dazhong Ma.

a low-impedance path between the battery and ground, and hundreds of amperes of current flow through the switching device, causing the device to burn. Owing to the limited size of the powerpack, the power semiconductor switching devices must have a smaller die size, which further reduces their SC capability [9], [10]. In the EOP powerpack connected to the 12-V battery, the automotive metal oxide semiconductor field-effect transistor (MOSFET) with drain-source breakdown voltage of 40 V is primarily used as a switching device. Generally, for an SC-withstand time, the motor can withstand for a few milliseconds to a few seconds; however, the MOSFET can only withstand for a few microseconds [11]–[14].

Protection methods against overcurrent or SC fault have been proposed in numerous previous studies. There are methods of directly measuring current using a shunt resistor or a current sensor [15]–[18], monitoring the change of di_d/dt [19]–[22], monitoring the gate-source voltage and gate charge characteristics [23] and using sense FET or a current mirror [24], [25]. Among these techniques, the most common method applied to the automotive three-phase low-voltage MOSFET driver circuit is the voltage from the drain to the source V_{ds} monitoring [26]–[30]. When an SC event occurs, the increasing drain current increases V_{ds} higher than the preset threshold voltage and a V_{ds} overvoltage (OV) fault is detected. However, this method requires a blanking time to prevent a false trigger [31], and because it senses the voltage rather than the drain current directly, it is not possible to protect with a preset current or to predict an accurate protection current [19], [27]. The fault detection level and peak SC current (SCC) level vary with the environmental operating temperature and load conditions that affect the MOSFET's temperature. A low-frequency and harmonic oscillation may also affect it [32]–[34]. Particularly in EOP powerpack applications, these drawbacks of the V_{ds} monitoring method may deteriorate the SC capability of MOSFET, which may lead to failure of protection or diagnosis. Because EOP powerpacks are located in a transmission, they are exposed to poor environmental conditions. In particular, in terms of operating temperature, the ATF's oil temperature around the powerpack is between 20°C and 120°C, and its ambient temperature is between −40°C and 130°C [35]. In the powerpack structure integrated into the motor, the ECU must be able to operate within a very wide range, from −40°C to 150°C, due to self-heating of the ECU and heat from the motor. In addition, the powerpack has various load profiles by changing the output of the pump and motor according to oil temperature change.

This study proposes a method to predict the SCC in V_{ds} monitoring and proposes a new protection method in which the SCC can be controlled within a certain protection range by applying the optimal fault threshold according to a wide operating temperature and various load conditions. When the proposed method is applied to the EOP powerpack, an improved diagnostic function with high quality can be provided. The rest of this article is organized as follows. In Section II, the causes of the change in the fault detection level of V_{ds} monitoring and the fluctuation in SCC are analysed. In addition, methods for determining the protection range for SCC and the filtering time of V_{ds} OV fault are theoretically derived through worst-case analysis. In Section III, to predict the SCC, the SCC waveform is estimated through circuit analysis, and the SCC map was derived. Further, to apply the optimal fault threshold according to various operating temperatures and load conditions, the on-resistance estimation method is discussed using simulation and experimental data. In Section IV, a new SC protection method with an adjustable fault threshold is proposed. The experiment results and the performance of the proposed method are verified in Section V. Finally, this article is concluded in Section VI.

II. AN SCC ANALYSIS

A. SCC FLUCTUATION IN V_{DS} MONITORING METHOD

The SC failure can be detected via a V_{ds} OV fault diagnostic method that compares the V_{ds} of the external MOSFET with the pre-selected V_{ds} OV fault threshold V_{dsth}. As is shown in Fig. 1(a), the SCB event occurs when the high-side MOSFET is shortened in one leg of the inverters and the low-side MOSET is turned on. The V_{ds} of the low-side MOSFET V_{ds_LS} is then increased by the SCC I_{sc}, which gradually increases over time, and then V_{ds_LS} becomes greater than V_{dsth}. At this point, the V_{ds} OV fault is detected and then the output voltage PWM of the gate drive circuit is turned off, and the current path between the battery and ground is cut off. In summary, when the SCB event occurs, V_{ds_LS} can be expressed as I_{sc} and the drain-source on-resistance of the MOSFET R_{dson}, as in equation (1), and the V_{ds} OV fault is detected when V_{ds_LS} is equal to V_{dsth}, as in equation (2):

$$V_{ds\_LS}(t) = I_{sc}(t) \times R_{dson} \tag{1}$$

$$V_{dsth} = V_{ds\_LS}(t_1) = I_{sc}(t_1) \times R_{dson} \tag{2}$$

Fig. 1(b) shows the change in the waveform of I_{sc} and the gate-source voltage V_{gs} waveform of low-side MOSFET. The upper current limit (UCL) and lower current limit (LCL) represent the minimum and maximum ranges of the SCC defined by the system specifications. Typically, the UCL is the maximum level of the SCC that the MOSFET can withstand. The LCL prevents normal current from being recognised as the SCC and its role is to prevent false fault detection; that is, the LCL is the maximum current value allowed by the system as a normal current. As is shown in the current curve of the black line in Fig. 1(b), the $I_{sc}(t_1)$ (when V_{ds_LS} is equal to V_{dsth} at t_1) is defined as an SC detection current I_{det}. The t_{qt} is a qualification time for detecting an intrinsic fault in order to prevent a false fault due to a temporary peak surge current. When it is determined that it is an intrinsic V_{ds} OV fault that is, after t_{qt}, the PWM output of the gate drive circuit is switched off, followed by the motor. The safety goal of the EOP powerpack is to avoid unintended operation of the pump and, when detecting a fault that violates a safety goal, it is reasonable to enter the inverter output disabled state because the defined

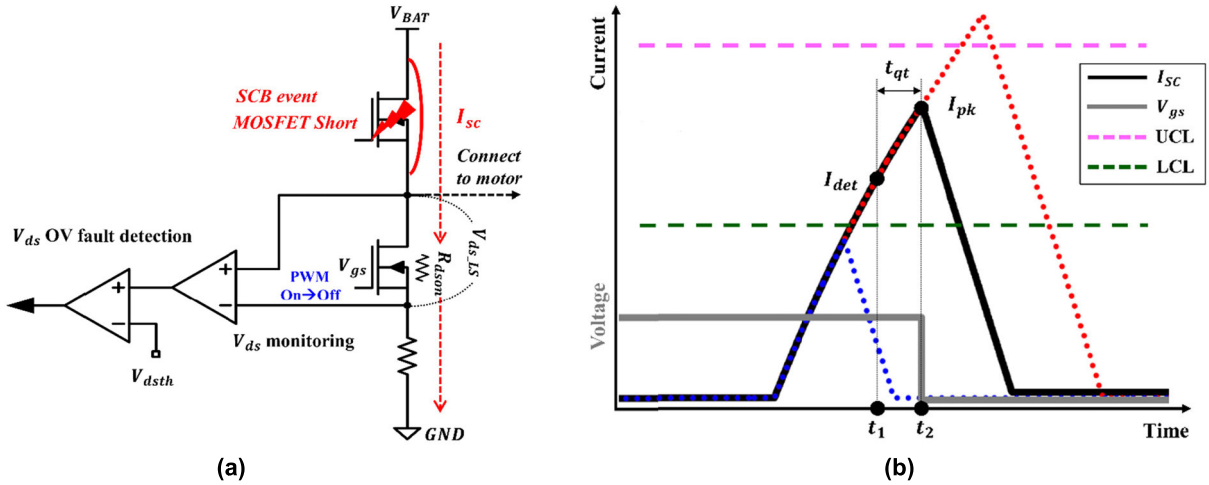

FIGURE 1. When the SCB event occurs: (a) V_{ds} OV fault detection circuit diagram of one of the inverter legs, (b) the waveforms of I_{sc} and V_{gs} of the low-side MOSFET.

safe state is a motor without torque. When the I_{sc} is cut off at t_2, the maximum current affecting the MOSFET is defined as a peak SCC I_{pk}. At t_2, the PWM output is also turned off, and so the V_{gs} of the low-side MOSFET drops to zero. The I_{pk} flowing through the low-side MOSFET is always larger than I_{det}. The V_{ds} OV fault detection mechanism in the SCG event is also operated similarly as the SCB case, where the low-side MOSFET is shortened and the fault can be detected in the high-side MOSFET. Therefore, except for SCG, this study is analysed and described based on the case of SCB event.

The factor that has the greatest influence on the fault threshold for SCs detection is the R_{dson} of MOSFET, as is described in equation (1). Most commercially-available MOSFETs feature at least twice the difference in R_{dson}, depending on the junction temperature T_j. The R_{dson} can be changed not only by T_j but also by the V_{gs}, the threshold voltage of the MOSFET V_{th}, and the drain current I_d. In general, however, the V_{gs}, supplied by the constant output voltage of the gate drive circuit with the charge pump does not change significantly with the temperature and the change in R_{dson} by I_d is also less than the change by T_j. Therefore, the change in T_j has the most influence on the change in R_{dson}. When an SC protection circuit has a pre-selected V_{dsth}, I_{det} and I_{pk} change due to the change in R_{dson} according to T_j. The blue and red dotted lines in Fig. 1(b) represent the waveforms of I_{sc} according to the change in $R_{dson}(T_j)$ when V_{dsth} is fixed. In the case of the blue dotted line, I_{det} decreases when the R_{dson} value increases, because T_j is high. Therefore, I_{pk} is not greater than LCL. In the case of the red dotted line, I_{det} increases when the R_{dson} value decreases, because T_j is low. Therefore, I_{pk} exceeds UCL. This figure shows that I_{det} and I_{pk} can vary significantly, according to $R_{dson}(T_j)$. As I_{pk} increases, the SC-withstand time of the MOSFET can gradually decrease, which may damage or deteriorate the MOSFET and, as the I_{det} decreases, the probability increases of misdiagnosing a normal peak current as the SCC.

This unpredictable SCC is dependent on $R_{dson}(T_j)$, increases the residual risk and reduces diagnostic coverage, which may not satisfy the functional safety requirements. It is necessary to reduce the deviation of I_{det} and I_{pk} according to the $R_{dson}(T_j)$, so that the SCC does not deviate from the specified diagnostic range under any operating conditions, thereby reducing the failure rate of the safety mechanism and the protection malfunction. To solve this problem, the V_{dsth} is not fixed but should be changed to an optimal fault threshold level according to $R_{dson}(T_j)$, and I_{det} and I_{pk} can be constantly controlled regardless of the influence of temperature and load conditions.

B. DETERMINATION OF THE PROTECTION RANGE

To select the optimal fault threshold, the minimum and maximum range of the SCC had to be determined. The allowable range of the SCC is defined by the UCL and LCL. The UCL is the maximum current that the SCC must not exceed for the protection of the MOSFETs, and LCL is the minimum current that should be diagnosed as the SCC. Therefore, the UCL relates to I_{pk} and LCL to I_{det}.

The UCL is based on the maximum I_{pk} without any damage to the MOSFET and the SCC must not exceed the UCL. The current limit without damage to the MOSFET may vary depending on the temperature, but the T_j can change rapidly, depending on the load current, and it is difficult to consider the UCL separately for every change in the T_j, and so the worst-case condition is assumed and selected. And, due to the distribution or error in the characteristics of mass parts, a safety margin is required to secure the stability of all parts. The allowable level and duration of the SCC that can flow to the MOSFET relate to the maximum operating temperature of the MOSFET and the thermal capacity of

TABLE 1. Mosfet parameters required for calculating equation (3).

Symbol	Parameter	Value	Unit	Data sources
$T_{j.max}$	Maximum operating junction temperature of MOSFET	175	°C	MOSFET datasheet [a]
$T_{c.max}$	Maximum case temperature of MOSFET	150	°C	Thermal measurement result
$R_{dson.max}$	Maximum drain-to-source on-resistance	3.23	mΩ	MOSFET datasheet [a]
t_p	Pulse width	50	μs	Assume maximum period
$Z_{th(j-c)}(t_p)$	Transient thermal impedance, junction to case at t_p	0.09	°C/W	MOSFET datasheet [a]
S_M	Safety margin	0.2	-	Assume 20%

[a]Refer to the datasheet of MOSFET AUIRF8736M2TR [36]

the package or die. The allowable instantaneous drain pulse current I_{dp} capability can then be calculated via equation (3), considering the worst-case:

$$I_{dp} = \sqrt{\frac{T_{j.max} - T_{c.max}}{R_{dson.max} \times Z_{th(j-c)}(t_p)}} \times (1 - S_M) \qquad (3)$$

The parameters related to equation (3) are shown in Table 1. The $T_{c.max}$ was considered the maximum case temperature in the worst-case operating condition, and the case temperature was measured by attaching thermal couplers. The $T_{c.max}$ was then saturated to 150°C under worst-case load condition. The SCC is generally in the form of a triangular pulse waveform but, assuming the worst-case condition, it was assumed to be a single rectangular pulse waveform and the pulse width t_p of the SCC was assumed to be 50 μs or less. The $Z_{th(j-c)}$ (t_p =50 μs) was known from the transient thermal impedance curves of the MOSFET datasheet [36], and the safety margin was assumed to be 20%. As the I_{dp} calculation result of equation (3), the UCL was determined to be 235 A.

The LCL is based on the minimum I_{det} that can be considered the SC failure, and the LCL should be selected with a safety margin above the maximum operating peak motor current flowing through the MOSFETs for short durations. The instantaneous current, generated when a very high torque is instantaneously required or when the brake mode is required, should be regarded as the normal operating current and not the SCC. The peak current required for normal operation should not be incorrectly sensed as the SCC. When considering all of the overall motor current profile for the various load points in the EOP powerpack, the LCL was determined in this study to be 140 A.

C. DETERMINATION OF THE QUALIFICATION TIME

In addition to selecting the allowable range of the SCC, the filtering time t_{qt} to confirm the fault was required for improving the accuracy of the diagnosis. After the SC detection and t_{qt} had expired, the V_{ds} OV fault could be confirmed and the SCC shut-off reaction occurred. Fig. 2(a) shows a simplified gate drive circuit that outputs the gate voltage to the external MOSFETs.

To select the optimal t_{qt}, other fault monitoring functions than the V_{ds} monitoring must be considered. The voltages of the external MOSFET to be monitored, which the gate drive circuit must monitor for diagnostic purposes, include not only V_{ds} but also V_{gs}, as is shown in Fig. 2(a). The V_{ds} monitoring is used for detecting SCs, whereas the V_{gs} monitoring ensures that sufficient gate voltage is provided to the MOSFET [37]–[39]. The V_{gs} undervoltage (UV) fault is to diagnose that the gate drive voltage is sufficient to fully turn on the external MOSFETs. In order to reduce the design cost and complexity of gate driver circuit, the same filtering time t_{qt} can be applied to the V_{ds} OV fault and V_{gs} UV fault detection [39]. The SCC can then be increased rapidly over an extremely short time-frame. In terms of SC detection, as the I_{pk} can be reduced as t_{qt} becomes shorter, it can be better assured to prevent damage or deterioration of MOSFETs. However, if the t_{qt} is too short, the gate drive voltage does not exceed the defined V_{gs} UV fault threshold voltage level and the V_{gs} UV fault flag will become active. That is, the selection of the t_{qt} features a trade-off between the V_{ds} OV fault and the V_{gs} UV fault detection.

In Fig. 2(b), V_{gsth} is the V_{gs} UV fault threshold voltage level and the time when the V_{gs} rises to V_{gsth} is defined as t_{gs_uv}. The $v_{gs}(t)$ is the time-varying gate to the source voltage. The left-hand side of Fig. 2(b) shows that the V_{gs} UV fault flag is activated because t_{qt} is less than t_{gs_uv} ($v_{gs}(t_{qt})$ is less than V_{gsth}), whereas the right-hand side of Fig. 2(b) shows that the V_{gs} UV fault flag is not activated because t_{qt} is longer than t_{gs_uv} ($v_{gs}(t_{qt})$ is greater than V_{gsth}). In other words, if t_{qt} is selected to be shorter than t_{gs_uv} to reduce I_{pk}, the functionality of the diagnostic will not work properly due to an unintended V_{gs} UV fault flag interrupt. The t_{qt} should be selected to at least be larger than the t_{gs_uv}, but the t_{gs_uv} can be changed by several characteristic parameter values related to the MOSFET turn-on. The t_{gs_uv} must then be calculated through the worst-case analysis with the minimum and maximum values of each parameter, with the longest t_{gs_uv} being used as the criterion for selecting the t_{qt}. As is shown in Fig. 2(c), t_{gs_uv} includes the sum of the periods of T_A, T_B and T_C. The t_3 is the time point at which $v_{gs}(t)$ becomes V_{gsth}. V_{gp} is the gate plateau voltage. To calculate each period of T_A, T_B and T_C, a simple equivalent circuit

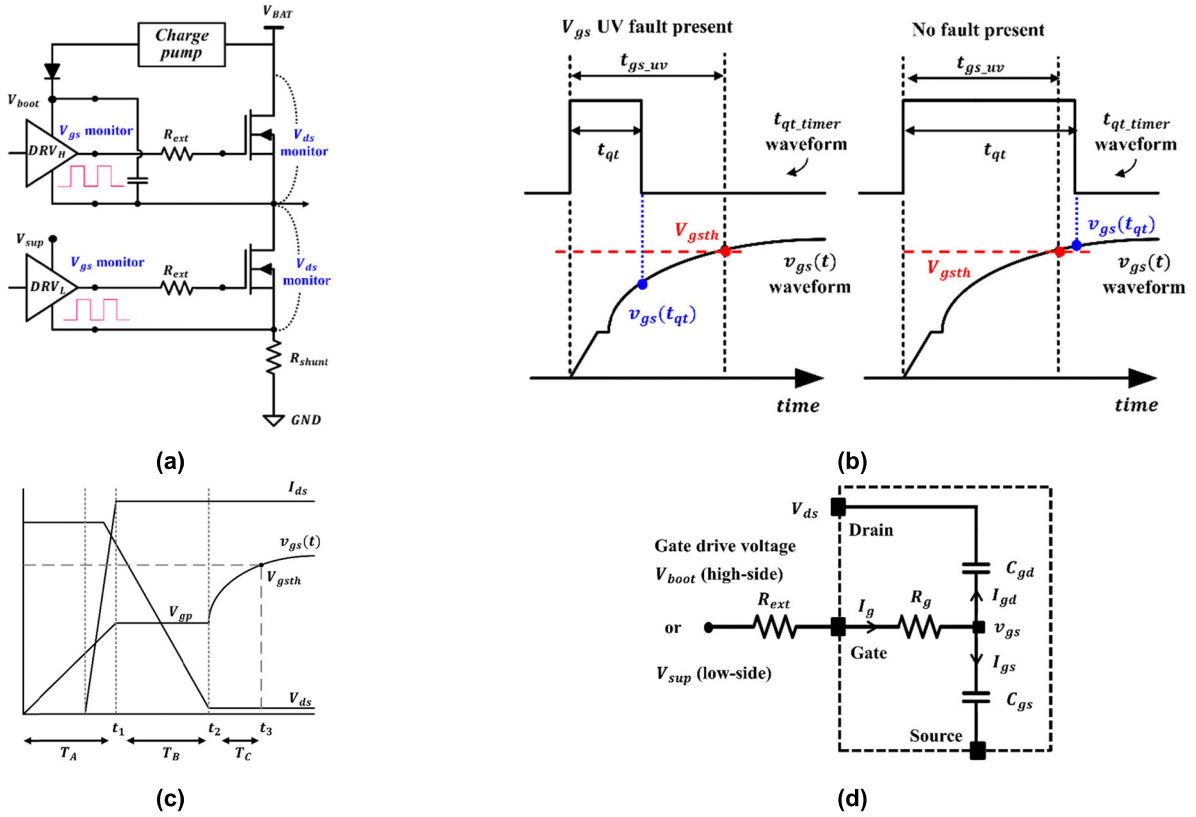

FIGURE 2. Analysis required to determine qualification time: (a) simplified circuit of the gate drive output and one of the inverter legs, (b) waveform comparison of the qualifying timer and $v_{gs}(t)$ based on the presence or absence of faults, (c) turn-on transient of the MOSFET and (d) simplified circuit from the gate drive output to the MOSFET gate equivalent model.

TABLE 2. Parameters related to the turn-on MOSFET.

Symbol	Description	Unit	Minimum value	Typical value	Maximum value
R_{g_tot}	$R_{ext} + R_g$	Ω	22.257	24.730	27.203
V_{boot}	Gate drive output voltage of the high-side	V	8.0	10.3	11.3
V_{sup}	Gate drive output voltage of the low-side	V	9.0	11.0	11.7
V_{gsth_H}	High-side V_{gs} UV threshold level (when V_{boot}=8.0 V)	V	6.75	7.00	7.20
	High-side V_{gs} UV threshold level (when V_{boot}=10.3 V)	V	9.05	9.30	9.50
	High-side V_{gs} UV threshold level (when V_{boot}=11.3 V)	V	10.05	10.30	10.50
V_{gsth_L}	Low-side V_{gs} UV threshold level (when V_{sup}=9.0 V)	V	7.75	8.00	8.20
	Low-side V_{gs} UV threshold level (when V_{sup}=11.0 V)	V	9.75	10.00	10.20
	Low-side V_{gs} UV threshold level (when V_{sup}=11.7 V)	V	10.45	10.70	10.90

Other parameters include the following values: C_{gs}= 10.13 nF, C_{gd}= 4 nF, $C_{iss(V_{gs}=0)}$= 6.867 nF, V_{gp}= 4.5 V, V_{ds}= 13.5 V.
For gate drive output voltages and V_{gs} UV threshold levels, refer to the datasheet of gate driver IC A4911 [39].

considering the parameters related to the turn-on transient of MOSFET is shown in Fig. 2(d). V_{boot} and V_{sup} are the gate output voltage of the high-side and low-side driver, R_{ext} and R_g are the external and internal gate resistance of MOSFET, C_{gs} and C_{gd} are gate-source and gate-drain capacitance. The formulas for T_A, T_B and T_C can be derived through the process of charging the gate from the equivalent circuit [40]. $T_A(0 - t_1)$, $T_B(t_1 - t_2)$ and $T_C(t_2 - t_3)$ can be calculated by means of equations (4)–(9) in both the high-side (T_{A_HS}, T_{B_HS}, T_{C_HS}) and low-side cases (T_{A_LS}, T_{B_LS}, T_{C_LS}). The parameters of equations (4)–(9) and their minimum and maximum values are listed in Table 2.

$$T_{A\_HS} = R_{g\_tot} C_{gs} \times \ln\left(\frac{1}{1 - \frac{V_{gp}}{V_{boot}}}\right) \tag{4}$$

TABLE 3. The calculation results of the worst-case analysis.

Symbol	Description	Unit	Minimum t_{gs_uv} [a]	Typical t_{gs_uv} [b]	Maximum t_{gs_uv} [c]	Comments
T_{A_HS}	High-side T_A	ns	115	144	228	From equation (4)
T_{B_HS}	High-side T_B	ns	177	230	420	From equation (6)
T_{C_HS}	High-side T_C	ns	259	299	276	From equation (8)
t_{gs_uvH}	$T_{A\_HS} + T_{B\_HS} + T_{C\_HS}$	ns	550	673	923	Maximum t_{gs_uvH} : 923 ns
T_{A_LS}	Low-side T_A	ns	110	132	191	From equation (5)
T_{B_LS}	Low-side T_B	ns	167	205	326	From equation (7)
T_{C_LS}	Low-side T_C	ns	268	318	323	From equation (9)
t_{gs_uvL}	$T_{A\_LS} + T_{B\_LS} + T_{C\_LS}$	ns	544	655	840	Maximum t_{gs_uvL} : 840 ns
t_{gs_uv}	$t_{gs\_uvH} + {t_{d1}}^d + {t_{d2}}^d$	ns	1020	1143	1393	t_{qt} > maximum t_{gs_uv}
	$t_{gs\_uvL} + t_{d1} + t_{d2}$	ns	1014	1125	1310	

[a]The combination conditions of the min-max parameters were as follows: V_{boot}= 11.3 V, V_{sup}= 11.7 V, V_{gsth_H}= 10.05 V, V_{gsth_L}= 10.45 V, R_{tot}= 22.257 Ω.
[b]The combination conditions of the min-max parameters were as follows: V_{boot}= 10.3 V, V_{sup}= 11 V, V_{gsth_H}= 9.3 V, V_{gsth_L}= 10 V, R_{tot}= 24.73 Ω.
[c]The combination conditions of the min-max parameters were as follows: V_{boot}= 8 V, V_{sup}= 9 V, V_{gsth_H}= 7.2 V, V_{gsth_L}= 8.2 V, R_{tot}= 27.203 Ω.
[d]The t_{d1} is the system clock error and the value is approximately 5% of the period t_{qt}, and the t_{d2} is the delay time of the comparators for V_{ds} OV or for V_{gs} UV fault detection, where max. t_{d1}= 70 ns and max. t_{d2}= 400 ns were assumed herein.

$$T_{A\_LS} = R_{g\_tot} C_{gs} \times \ln\left(\frac{1}{1 - \frac{V_{gp}}{V_{sup}}}\right) \tag{5}$$

$$T_{B\_HS} = R_{g\_tot} C_{gd} \times \frac{V_{ds}}{V_{boot} - V_{gp}} \tag{6}$$

$$T_{B\_LS} = R_{g\_tot} C_{gd} \times \frac{V_{ds}}{V_{sup} - V_{gp}} \tag{7}$$

$$T_{C\_HS} = R_{g\_tot} C_{iss(V_{gs}=0)} \times ln\left(\frac{V_{boot} - V_{gp}}{V_{boot} - V_{gsth\_H}}\right) \tag{8}$$

$$T_{C\_LS} = R_{g\_tot} C_{iss(V_{gs}=0)} \times ln\left(\frac{V_{sup} - V_{gp}}{V_{sup} - V_{gsth\_L}}\right) \tag{9}$$

From −40°C to 150°C operating temperatures, variations in the electrical characteristics of each drive output voltage, total gate resistance, and variations in the V_{gsth} for each drive output voltage were applied. The maximum values were applied for C_{gs}, C_{gd} and $C_{iss(V_{gs}=0)}$, and fixed values were applied for V_{gp} and V_{ds}. With the minimum, typical and maximum values of the gate resistances, the gate drive output voltages and V_{gsth} values at high-side and low-side, T_A, T_B and T_C were calculated as all combinable cases, and the values of t_{gs_uv} were derived for the high-side and low-side cases. Among the combinations of several cases, Table 3 shows cases in which the minimum, typical and maximum values of t_{gs_uv} were derived. In calculating the value that t_{qt} should exceed at least not only t_{gs_uv} but also delay time, such as the system clock error t_{d1} and delay of the comparator for fault detection t_{d2}. Considering the maximum value of t_{gs_uv} and the delay times t_{d1} and t_{d2}, the t_{qt} must be longer than 1393 ns. Therefore, the optimal t_{qt} was determined to be 1.4 μs. The gate drive output could be shut off after 1.4 μs from the SC detection.

III. AN SCC PREDICTION AND $R_{DSON}(T_J)$ ESTIMATION

A. SCCW ESTIMATION

Previously, the diagnostic range and qualification time of the SCC were determined, but the appropriate V_{dsth} for I_{det} and I_{pk} remain to be determined, which varies depending on the $R_{dson}(T_j)$. If the SCC waveform (SCCW) can be formally and mathematically estimated, the I_{det} and I_{pk} values can be predicted according to $R_{dson}(T_j)$. To estimate the SCCW, Fig. 3(a) illustrates a simplifying inverter equivalent circuit when considering the SCB event situation. When an SC event occurs, the energy of the rapidly increasing $I_{sc}(t)$ curve can be supplied from the DC-link's large aluminium electrolytic capacitor.

As is shown in Fig. 3(b), the quantity of electric charge Q required to increase the current to a maximum I_{pk} ($I_{pk.max}$) within t_{cut} can be calculated from equation (10). And, in Fig. 3(a), the high-side MOSFET was shortened and, when the low-side MOSFET was turned on, a low impedance is formed between the bridge voltage V_{BAT} and ground, and the $I_{sc}(t)$ rapidly increased, so that the V_{BAT} dropped at the same time. When the voltage drop of the V_{BAT} was defined as the ΔV_{dp}, as is shown in Fig. 3(b), ΔV_{dp} can be expressed by equation (11). From this, the minimum capacitance C_{min} that can provide Q during t_{cut} can be derived as equation (12). Here, $I_{pk.max}$ was assumed to be 300 A in the worst-case, t_{cut} was assumed to be 15 μs, the allowable ΔV_{dp} was assumed to be 5 V (in this study, the nominal battery voltage was 13.5 V and the minimum operating guarantee voltage of was 8.5 V, in other words, the ECU can guarantee full performance even if the V_{BAT} is reduced to 8.5 V) and the equivalent series resistance (ESR) of the DC-link capacitor was 14 mΩ. Then, C_{min} was calculated as 2813 μF.

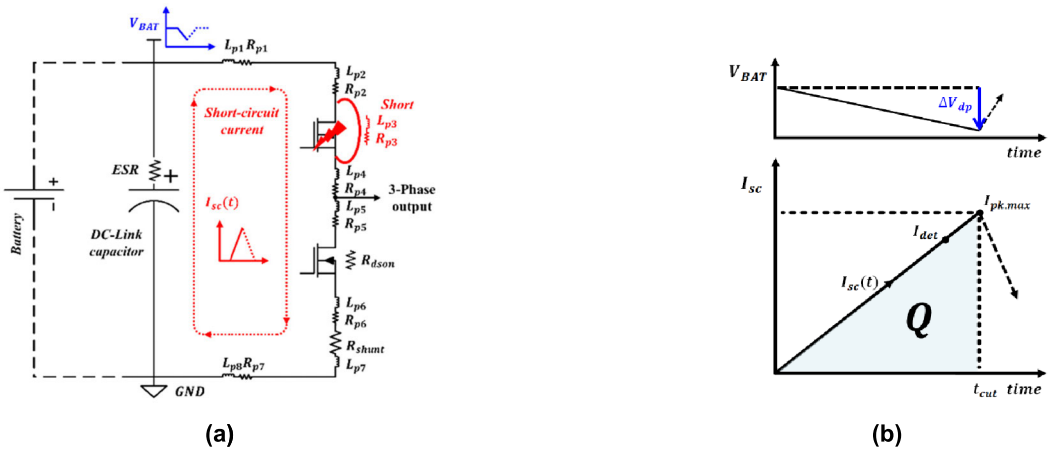

FIGURE 3. When the SCB event occurs: (a) simplified inverter equivalent circuit, (b) I_{sc} rising curve and bridge voltage V_{BAT} waveform.

The DC-link's large capacitance was then applied to the EOP powerpack as 3900 μF, which was determined to be sufficient current source for the increase in $I_{sc}(t)$.

$$Q = \frac{1}{2} I_{pk.max} t_{cut} \tag{10}$$

$$\Delta V_{dp} = I_{pk.max} \times ESR + \frac{Q}{C_{min}} \tag{11}$$

$$C_{min} = \frac{Q}{\Delta V_{dp} - I_{pk.max} \times ESR} \tag{12}$$

In the event of an SC, the remainder of the circuit, except for the large capacitance, becomes an *RL* circuit that comprises the parasitic resistances and inductances of the PCB pattern, the R_{dson} of the MOSFET and the resistance and parasitic inductance of the shunt resistor. The $I_{sc}(t)$ instantaneously increases in a similar fashion to a rising curve with the *RL* time constant.

On the basis of the circuit analysis, the SPICE simulation was performed to estimate the time-varying current waveform when an SC event occurs during motor operation. As is shown in Fig. 4(a), the simulation scenario was as follows. While running the motor at 3000 rpm, the SC switch connecting the drain and source of the high-side MOSFET of the U-phase at t_{short} is forcibly closed. When the low-side FET of the U-phase is turned on by the operating mode of the 3-leg inverter, according to the switching state, SC detection will be performed and the SC reaction (V_{gs_LS} =0 V) activated after the filter time of t_{qt} 1.4 μs expires. Then, no current is freewheeling through the affected FET. As the defined safe state is a motor without torque, the gate drive circuit should turn off the affected MOSFET, as well as the other MOSETs. The simulated measuring point of I_{sc} was placed on the forced SC switch marked with second in Fig. 4(a). The waveform of the three-phase currents (I_u, I_v, I_w), I_{sc}, and V_{gs_LS} are shown in Fig. 4(b). As the simulation scenario, an SC event occurred at the point of t_{short} and the PWM voltage was then turned off, and I_{sc} was also cut-off.

Fig. 4(c) shows an enlarged view of the point where the SC event occurred in the simulated I_{sc} waveform, marked with "Zoom in I_{sc}" in Fig. 4(b). And, how the I_{det} and I_{pk} values change according to T_j was also simulated, and the SCCW was graphed. It was assumed that the *RL* time constant do not change with T_j, but the R_{dson} changes with T_j. The triangular waveform graphs of I_{sc} were estimated using the curve fitting method based on the simulation results for each case, with V_{dsth} from 350 mV to 500 mV at 50 mV intervals and T_j spanning 20°C to 150°C. In Fig. 4(c), SCCWs are divided into four groups according to the V_{dsth} values, and within one group, they are graphed according to the change of T_j. The I_{det} values can be calculated and predicted with pre-set V_{dsth} and R_{dson} values, but it is difficult to estimate and predict the I_{pk} values. However, the I_{pk} values can be obtained through the SCCW graphs. The current value after 1.4 μs from I_{det} (= $I_{sc}(t_{det})$) point becomes I_{pk} (= $I_{sc}(t_{pk})$).

In the SCCW graphs, for instance, when the V_{dsth} is 500 mV, the maximum and minimum of the I_{det} were, respectively, 231 A at T_j =20°C and 154 A at T_j =150°C, and the maximum and minimum of the I_{pk} were 286 A at T_j =20°C and 220 A at T_j =150°, respectively. The results indicate that the I_{det} can vary up to 77 A and that the I_{pk} can vary up to 66 A depending on the T_j under the same V_{dsth}. It has been found that the SCCWs have a very wide distribution at fixed and same V_{dsth}.

B. DERIVATION OF SCC MAP AND VARIABLE V_{DSTH}

The I_{det} and I_{pk} values, according to each V_{dsth} and T_j, can be obtained through the SCCW graphs. With the simulated and estimated values, the SCC map can be derived as shown in Table 4. The T_j ranges from 20°C to 150°C, but the cold temperature range was excluded because the oil temperature around the powerpack is maintained from 20°C to 120°C and the heatsink temperature distribution for the ECU is in the range of 20°C or more and occupies more than 95% of the total lifetime. And, as is shown in Fig. 4(a), the monitoring

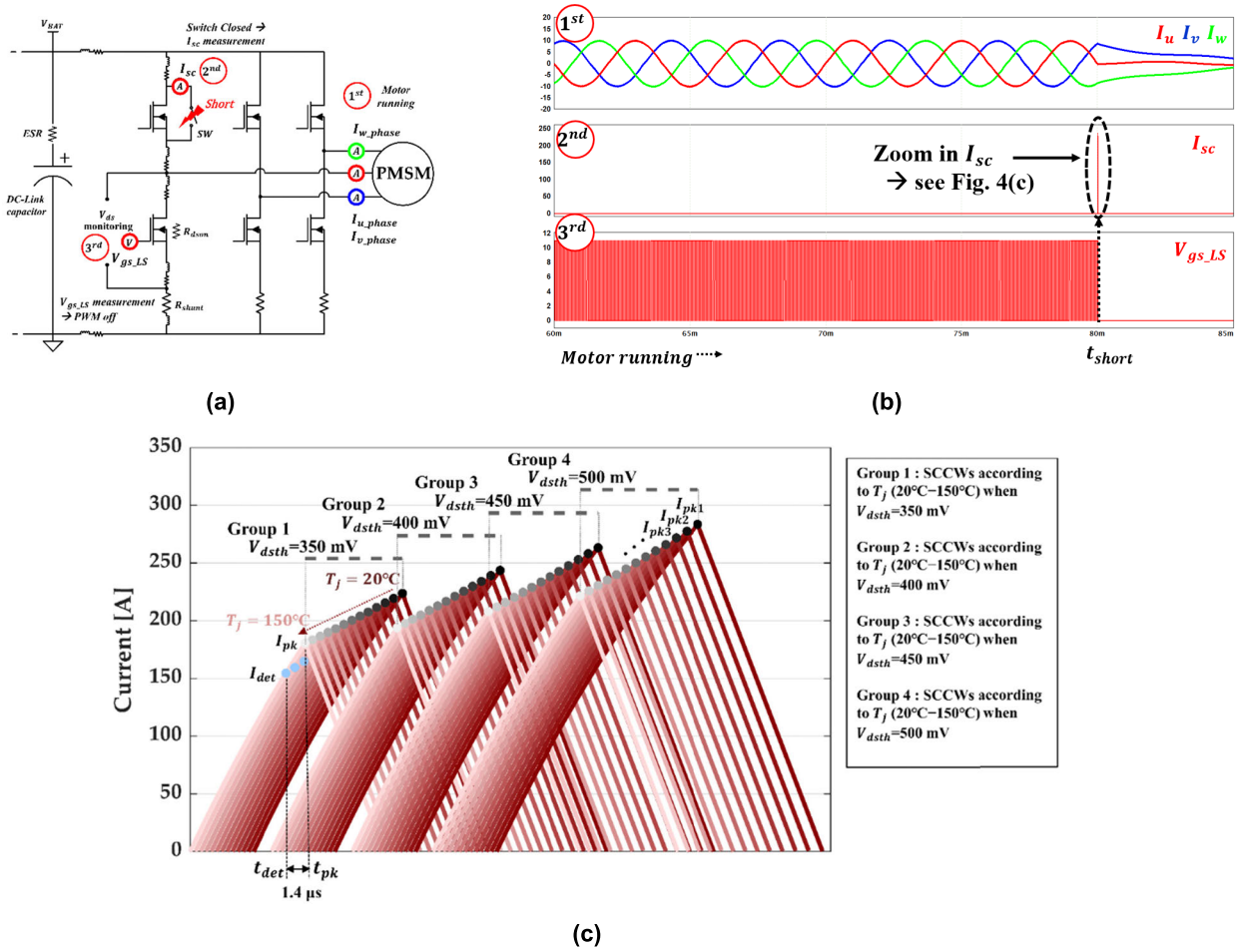

FIGURE 4. SCCW estimation: (a) simulation schematic, (b) simulation waveforms of the phase currents (I_u, I_v, I_w), SCC (I_{sc}), and V_{gs} of the low-side MOSFET (V_{gs_LS}) and (c) SCCW graphs according to V_{dsth} and T_j.

points of the V_{ds} OV fault are not exactly the drain and source points of the MOSFET, and it may depend on the PCB design, but usually the motor phase voltage output point and the point between the source pin of MOSFET and shunt resistor. The R_{dson} is merely the resistance between the source pin and drain contact of the surface-mount type MOSFET. Therefore, in addition to the R_{dson}, the parasitic resistances, such as the soldering contact resistance and PCB pattern resistance to monitor V_{ds} should be considered together. In this paper, the additional 0.3 mΩ of parasitic resistance R_p was assumed. Table 4 summarises the I_{det} and I_{pk} values for 20°C–150°C in 5°C increments and the V_{dsth} from 350 mV to 500 mV in 50 mV increments.

In the EOP application, the ECU receives the target speed command from the transmission control unit and performs torque maintenance control functions when the speed reaches its specified level, and so the motor current and speed do not change rapidly over short moments. Typically, in the load current profile of the EOP, the magnitude of the motor current can be maintained for a few seconds to a few tens of minutes. Therefore, there is enough time to estimate the T_j change and again set V_{dsth} value according to the T_j.

Changing the V_{dsth} settings for every too short T_j change, such as the 1°C interval, can lead to increased computational processing unit load. Moreover, as is shown in Table 4, for changes in T_j of less than 10°C, the difference in I_{det} and I_{pk} is not as large as 10 A or less. As is shown in the grey blocks in Table 4, the entire temperature range of 20°C–150°C of T_j was divided into four temperature zones. To reduce the wide fluctuation range of I_{det} and I_{pk}, each different V_{dsth} settings are applied according to the each of four temperature zones. The V_{dsth} values are determined to be 350 mV at 25°C–50°C, 400 mV at 50°C–90°C, 450 mV at 90°C–125°C, and 500 mV at 125°C–150°C. If the T_j is estimated to be over 150°C, an over-temperature fault will be generated and the EOP powerpack will notify the transmission control unit to be on standby mode via CAN communication without further driving the motor.

Fig. 5(a) and (b) shows the comparison of the change in the I_{det} and I_{pk} values according to T_j when V_{dsth} was

TABLE 4. Summary of the SCC map.

T_j(°C)	R_{dson} (mΩ)	R_{dson_P} (mΩ)	V_{dsth}=350 mV		V_{dsth}=400 mV		V_{dsth}=450 mV		V_{dsth}=500 mV	
		$R_{dson}+R_p$[a]	I_{det}[A]	I_{pk}[A]	I_{det}[A]	I_{pk}[A]	I_{det}[A]	I_{pk}[A]	I_{det}[A]	I_{pk}[A]
20	1.867	2.167	162	226	185	246	208	266	231	286
25	1.900	2.200	159	224	182	244	205	263	227	284
30	1.933	2.233	157	222	179	241	201	261	224	281
35	1.968	2.268	154	220	176	239	198	258	221	278
40	2.002	2.302	152	217	174	237	195	256	217	274
45	2.038	2.338	150	216	171	234	193	253	214	272
50	2.073	2.373	147	213	169	232	190	251	211	269
55	2.110	2.410	145	212	166	230	187	248	208	266
60	2.147	2.447	143	209	163	228	184	245	204	263
65	2.185	2.485	141	208	161	226	181	243	201	260
70	2.223	2.523	139	206	159	223	178	241	198	258
75	2.263	2.563	137	204	156	221	176	238	195	255
80	2.303	2.603	134	202	154	219	173	236	192	253
85	2.343	2.643	132	200	151	217	170	234	189	250
90	2.384	2.684	130	199	149	215	168	231	186	248
95	2.426	2.726	128	197	147	213	165	229	183	245
100	2.469	2.769	126	195	144	211	163	227	181	242
105	2.513	2.813	124	193	142	209	160	225	178	240
110	2.557	2.857	123	192	140	207	158	222	175	238
115	2.602	2.902	121	190	138	205	155	220	172	235
120	2.648	2.948	119	189	136	203	153	218	170	233
125	2.695	2.995	117	187	134	201	150	216	167	231
130	2.742	3.042	115	185	131	200	148	214	164	229
135	2.790	3.090	113	183	129	198	146	212	162	226
140	2.840	3.140	111	182	127	196	143	210	159	224
145	2.890	3.190	110	181	125	194	141	208	157	222
150	2.941	3.241	108	179	123	192	139	206	154	220

[a] R_p is the parasitic resistance. It was assumed to be 0.3 mΩ.

fixed and V_{dsth} was changed according to the proposed SCC map. Fig. 5(a) shows that the fluctuations of I_{det} and I_{pk} across the entire temperature range are large, with some I_{pk} exceeding the UCL and some I_{det} being lower than the LCL. However, in Fig. 5(b), the fluctuations of I_{det} and I_{pk} across the entire temperature range are small, and I_{pk} and I_{det} are controlled within the UCL and LCL ranges. Based on the derived SCC map, it has been found that if V_{dsth} is controlled and programmable according to junction temperature, the I_{det} and I_{pk} can also be controlled.

C. $R_{DSON}(T_J)$ ESTIMATION

In order to change optimal V_{dsth} according to the proposed SCC map, it is important to accurately estimate $R_{dson}(T_j)$, which is the change criterion, according to the operating temperature and load conditions. In general, on-state resistance of the MOSFET can be expressed as a function T_j, as is shown in equation (13) [41]:

$$R_{dson}\left(T_j\right) = R_{dson}(25°\mathrm{C}) \times \left(1 + \frac{\alpha}{100}\right)^{T_j - 25°\mathrm{C}} \tag{13}$$

where α is a technology-dependent constant and has different values depending on the manufacturers and the MOSFET device types. The α was assumed to be 0.35. In equation (13), the slope of the $R_{dson}\left(T_j\right)$ is ultimately determined by the T_j values. As the MOSFET is packaged in an epoxy mould, it is difficult to directly measure the T_j values. Therefore, it may be estimated through the T_j thermal estimation model. The T_j can be expressed as equation (14), below:

$$T_j = T_{j\_start} + \Delta T_j = T_{ntc} + R_{j-ntc} \times P_{loss} \tag{14}$$

where T_{ntc} is the value transferred by converting the analogue output voltage from the negative temperature coefficient of resistance sensor (NTC) into temperature values and R_{j-ntc} is the thermal resistance between the junction and NTC. In the EOP application, the ECU must measure the temperature of the hotspot for over-temperature protection. In general, a temperature sensor such as an NTC is located near the six switching-MOSFETs and the hotspot temperature is sensed in real time. The T_{j_start} can be replaced with the sensing T_{ntc} values measured in real time. Moreover, ΔT_j is due to the self-heating of the MOSFET and can be calculated on the basis of the thermal resistance and power loss. The R_{j-ntc} was experimentally estimated, and this experimental principle approach to how the thermal impedance should be determined is well-known from previous studies [42], [43]. In order to determine R_{j-ntc}, the temperature rise difference between the junction and NTC ΔT_{j-ntc} should be

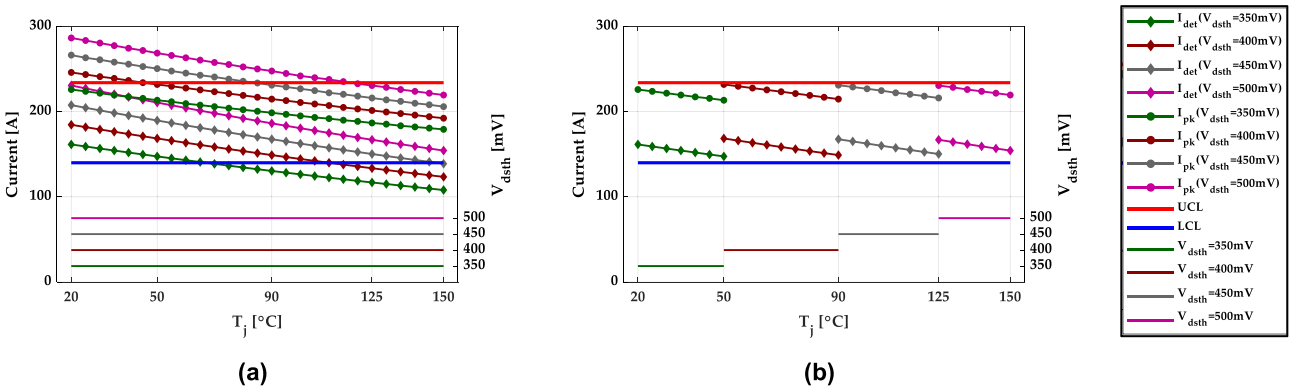

FIGURE 5. Change of I_{det} and I_{pk} with T_j: (a) when V_{dsth} was fixed at 350, 400, 450 and 500 mV, (b) when V_{dsth} changes from 350 mV to 500 mV in 50 mV increments.

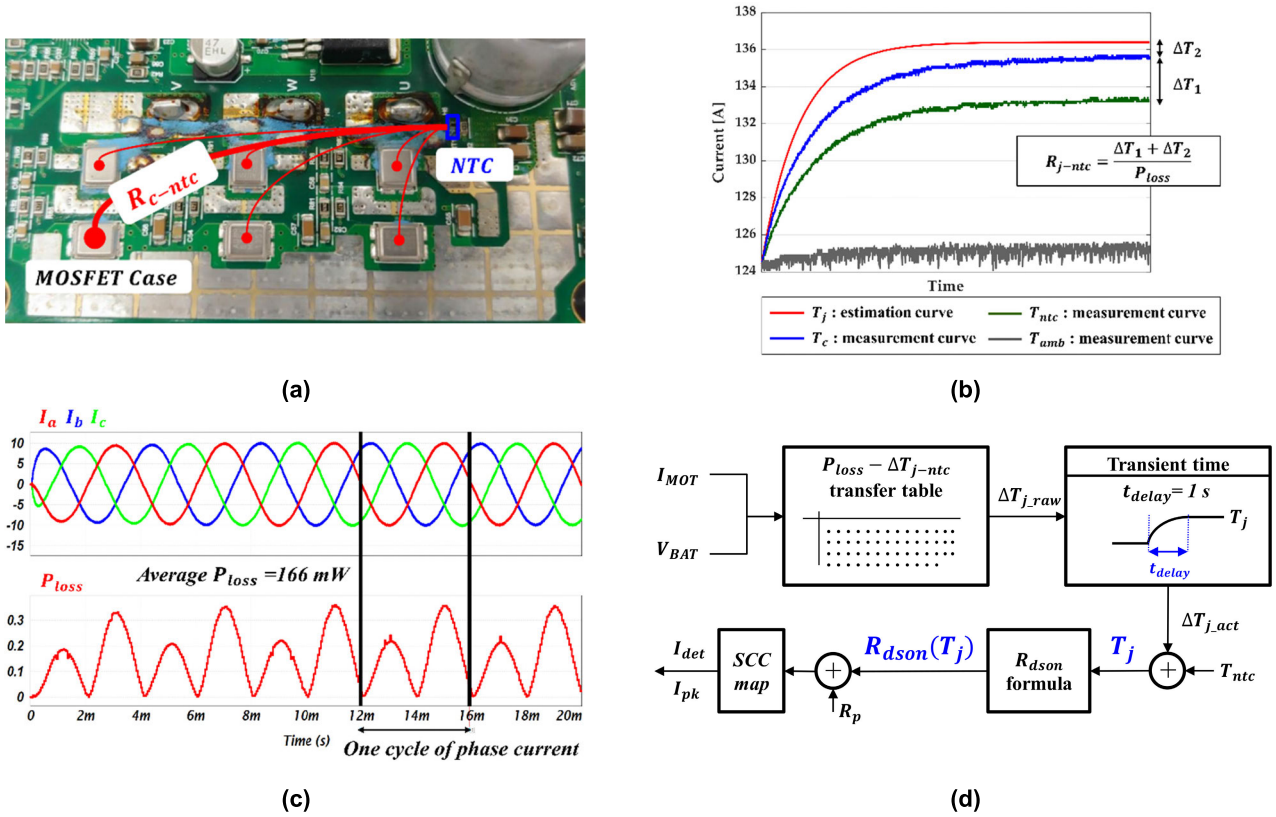

FIGURE 6. $R_{dson}(T_j)$ estimation: (a) layout of the NTC and six switching-MOSFETs, (b) thermal measurement results of NTC and T_c, and estimated T_j graph when driving with motor current 10 A, (c) simulation result of P_{loss} at V_{BAT} = 13.5 V and I_{MOT} = 10 A and (d) the block diagram of the $R_{dson}(T_j)$ calculation module.

obtained after applying a constant power loss P_{loss}. In order to obtain ΔT_{j-ntc}, the temperature rise difference should be divided into ΔT_{c-ntc} (between the case and NTC) and ΔT_{j-c} (between the junction and case).

As is shown in Fig. 6(a), as the ΔT_{c-ntc} values have the deviation according to the PCB layout location of each of the six switching-MOSFETs and PCB design, the worst-case ΔT_{c-ntc} was considered. In order to obtain ΔT_{c-ntc} through the thermal measurement, when a continuous constant driving with a 10 A motor current at an ambient temperature T_{amb} of 125°C, the P_{loss} of 166 mW was consumed in the MOSFET and T_{ntc} and T_c were measured until saturation had been reached. The measured graphs of T_{amb}, T_{ntc}, and T_c are shown in Fig. 6(b). At that point in time, the measured $\Delta T_{c-ntc}(= \Delta T_1)$ was measured at 2.08°C. As the temperature difference between the junction and case, $\Delta T_{j-c}(= \Delta T_2)$ is difficult to measure, it was estimated with the R_{j-c} value 2.4°C/W obtained from the transient thermal

TABLE 5. $P_{loss} - \Delta T_{j-ntc}$ transfer table.

V_{BAT}		9.5 [V]		10.5 [V]		11.5 [V]		12.5 [V]		13.5 [V]		14.5 [V]		15.5 [V]	
I_{MOT} [A]	T_{amb}	P_{loss} [mW]	ΔT_{j-ntc} [°C]	P_{loss} [mW]	ΔT_{j-ntc} [°C]	P_{loss} [mW]	ΔT_{j-ntc} [°C]	P_{loss} [mW]	ΔT_{j-ntc} [°C]	P_{loss} [mW]	ΔT_{j-ntc} [°C]	P_{loss} [mW]	ΔT_{j-ntc} [°C]	P_{loss} [mW]	ΔT_{j-ntc} [°C]
.	.	.	.	The rest was omitted.[a]								.	.	.	.
.	.	.	.									.	.	.	.
7	RT	74.7	1.11	79.2	1.18	84.8	1.26	91.3	1.36	97.8	1.46	104.4	1.55	111.9	1.67
	Hot	76.2	1.14	80.7	1.20	86.3	1.29	92.5	1.38	99.0	1.48	105.5	1.57	113.1	1.69
8	RT	89.4	1.33	95.9	1.43	102.0	1.52	108.6	1.62	116.3	1.73	124.8	1.86	133.2	1.98
	Hot	92.9	1.38	98.9	1.47	105.0	1.56	111.7	1.66	119.3	1.78	127.5	1.90	136.0	2.03
9	RT	106.7	1.59	112.8	1.68	120.4	1.79	128.8	1.92	136.6	2.04	145.8	2.17	155.6	2.32
	Hot	111.8	1.67	118.0	1.76	125.6	1.87	133.6	1.99	141.7	2.11	150.2	2.24	160.3	2.39
10	RT	124.1	1.85	132.5	1.97	139.8	2.08	148.9	2.22	159.0	2.37	169.0	2.52	179.5	2.67
	Hot	132.1	1.97	140.1	2.09	147.5	2.20	156.5	2.33	166.2	2.48	176.4	2.63	186.6	2.78
11	RT	144.4	2.15	152.0	2.26	162.1	2.42	171.6	2.56	181.8	2.71	193.4	2.88	205.1	3.06
	Hot	154.8	2.31	162.6	2.42	172.2	2.57	182.0	2.71	192.3	2.87	203.7	3.04	215.4	3.21
12	RT	165.4	2.46	174.8	2.60	184.1	2.74	196.0	2.92	207.4	3.09	219.2	3.27	232.9	3.47
	Hot	179.6	2.68	188.8	2.81	198.0	2.95	209.4	3.12	221.2	3.30	233.3	3.48	246.4	3.67
13	RT	189.0	2.82	198.0	2.95	209.7	3.12	220.8	3.29	234.8	3.50	248.3	3.70	262.6	3.91
	Hot	207.1	3.09	216.2	3.22	227.5	3.39	238.5	3.55	252.1	3.76	265.8	3.96	279.9	4.17
14	RT	213.5	3.18	225.1	3.35	235.8	3.51	249.4	3.72	263.0	3.92	279.1	4.16	294.7	4.39
	Hot	236.4	3.52	247.9	3.69	258.5	3.85	271.6	4.05	284.7	4.24	300.6	4.48	316.6	4.72
15	RT	240.6	3.58	252.6	3.76	265.8	3.96	279.6	4.17	294.7	4.39	311.0	4.63	329.4	4.91
	Hot	268.4	4.00	280.1	4.17	293.4	4.37	306.9	4.57	321.7	4.79	337.5	5.03	355.8	5.30
16	RT	270.2	4.03	283.7	4.23	297.6	4.43	312.6	4.66	329.2	4.91	346.8	5.17	365.8	5.45
	Hot	303.7	4.53	316.9	4.72	330.4	4.92	345.6	5.15	362.0	5.39	379.1	5.65	397.6	5.92
.	.	.	.	The rest was omitted.[a]								.	.	.	.
.	.	.	.									.	.	.	.

[a]Only partial examples of the P_{loss}-ΔT_{j-ntc} transfer table are shown.

impedance diagram of the MOSFET datasheet [36]. As the P_{loss} was 166 mW, the ΔT_{j-c} was calculated as 0.4°C. Therefore, the ΔT_{j-ntc} was estimated as 2.48°C and the R_{j-ntc} derived as 14.9°C/W. The T_j graph (red line) in Fig. 6(b) was estimated using the curve fitting method with the predicted transient thermal impedance [44].

The total P_{loss} of the MOSFET comprises the conduction and switching losses of the MOSET and those of the anti-parallel diode. As is shown in Fig. 6(c), the values of P_{loss} were simulated according to the load currents and the battery supply voltages with the real motor model parameters. The average power loss for one cycle of the current was simulated. As is shown in Table 5, the $P_{loss} - \Delta T_{j-ntc}$ transfer table was created so that the P_{loss} could be mapped to the temperature increase ΔT_{j-ntc} according to various battery supply voltage and motor currents, avoiding additional computational time. The P_{loss} and ΔT_{j-ntc} were considered at room temperature (RT: T_{amb} =25°C) and hot temperature (Hot: T_{amb} =125°C) with consideration of the performance deterioration of the MOSFET, such as the R_{dson}, according to the temperature. Fig. 6(d) shows the block diagram of the $R_{dson}(T_j)$ calculation module. The ΔT_{j-ntc} is mapped through the $P_{loss} - \Delta T_{j-ntc}$ transfer table based on the motor current and battery supply voltage measured in real time for motor control. At this time, the mapped ΔT_{j-ntc} value is saved as ΔT_{j_raw}. In practical applications, the temperature transient time t_{delay} due to the thermal capacitance factor must also be considered [45]. The temperature constant t_{delay} can differ by the MOSFET package type and thermal design of the PCB and heat sink. The t_{delay} was assumed to be 1 s herein. The ΔT_{j_raw} was recognised as the actual rising temperature ΔT_{j_act} after 1 s. The ΔT_{j_act} was then added to T_{ntc} and the final T_j calculated. Thereby, the $R_{dson}(T_j)$ could be calculated. Based on $R_{dson}(T_j)$, I_{det} and I_{pk} values mapped through the SCC map are derived and saved. Herein, the additional ΔT_{j-ntc} increased by the SCC after SCB event was neglected. This is because the total time (required by the automotive ECU) from the occurrence of the SC to the SCC cut-off is usually very short, such as a few microseconds.

IV. PROPOSED ONLINE SC PROTECTION METHOD WITH AN AUTOMATIC PROGAMMABLE FAULT THRESHOLD

A new online SC protection method was proposed to ensure that the SCC was not beyond the defined range UCL and LCL, regardless of the temperature change in the MOSFET according to the environmental temperature or load operating conditions. Thus far, in order to construct the protection method that automatically sets the variable V_{dsth} according to the T_j, the decision of the UCL and LCL, of t_{qt}, SCCW estimation, derivation of the SCC map and the $R_{dson}(T_j)$ calculation module were defined and analysed. The flowchart of the proposed protection method is shown in Fig. 7, below.

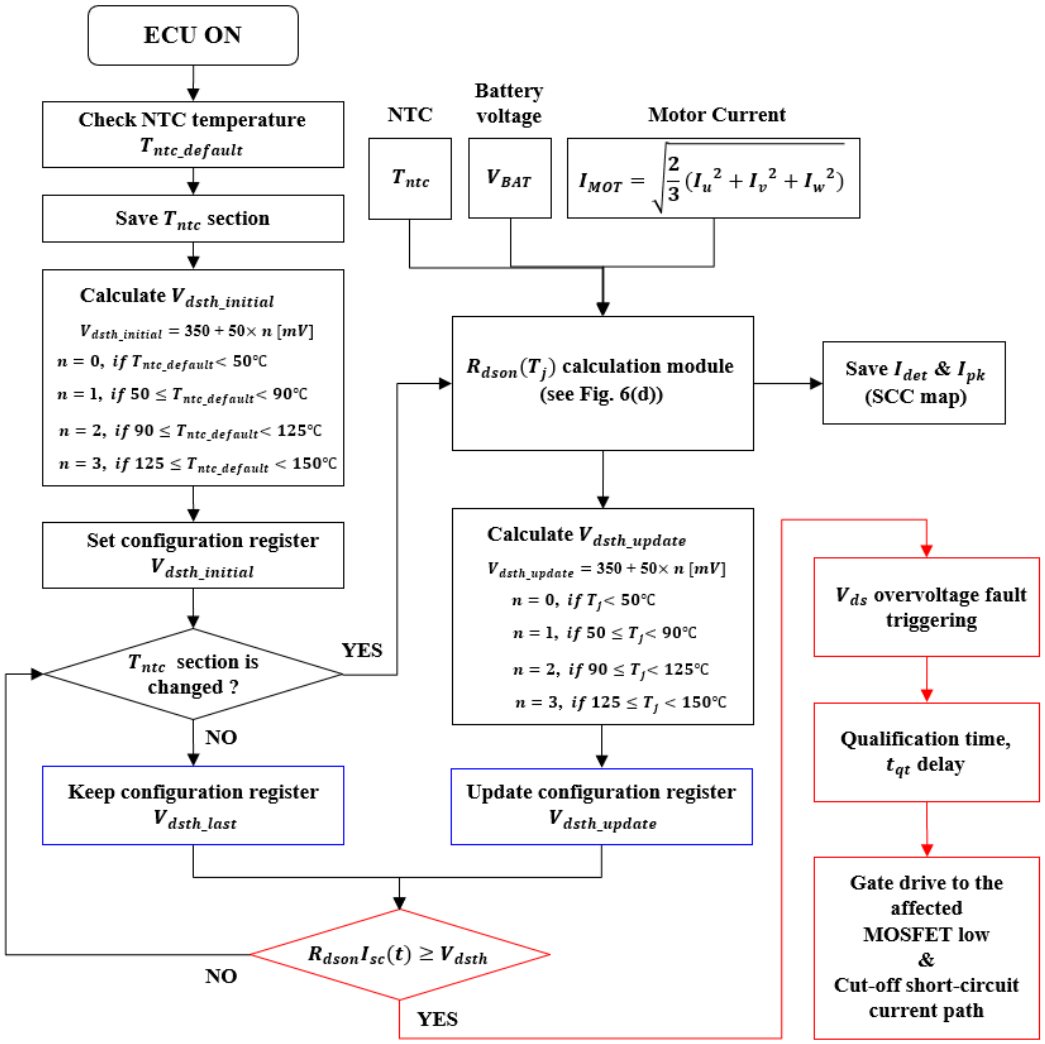

FIGURE 7. Flowchart of the proposed online SC protection method.

A detailed description of the flowchart of the proposed online SC protection method is as follows:

1) When the ECU is switched on, the PCB temperature is checked by the NTC located in the hotspot of the PCB and set as $T_{ntc\_default}$.
2) Based on $T_{ntc\_default}$, the entire operating temperature range from 20°C to 150°C is divided into 5°C intervals. At this point, each section divided every 5°C is defined as a T_{ntc} section. For instance, if the $T_{ntc\_default}$ is 35°C, one section spans from 32.5°C to 37.4°C and the next one from 37.5°C to 42.4°C. The sections are set to ignore instantaneous fluctuation in T_j. The range of all of the sections is saved.
3) The initial V_{dsth} is set with the $T_{ntc\_default}$. For instance, if $T_{ntc\_default}$ is 42°C, $V_{dsth\_initial}$ is 350 mV and if $T_{ntc\_default}$ is 55°C, $V_{dsth\_initial}$ is 400 mV. In this paper, the default value of the V_{dsth} is set to 350 mV, and the V_{dsth} values can be changed by an integer multiple of 50 mV depending on the $T_{ntc\_default}$. The calculated $V_{dsth\_initial}$ value is then set in the register.
4) After the $V_{dsth\_initial}$ is set, the T_{ntc} section change is monitored and, if the section is not changed, the current stored V_{dsth} value (V_{dsth_last}) is maintained and, if the section is changed, the $R_{dson}(T_j)$ calculation module is entered to set a new V_{dsth}. The reason why the V_{dsth} is controlled depending on whether the T_{ntc} section is changed or not is to exclude the sudden rise and fall of T_j as a result of temporary load fluctuations. Considering the load current profile or use-case of the EOP powerpack, the actual target operation period usually spans several seconds to thousands thereof. Even if an instantaneous T_j increase occurs, the T_j will immediately decrease because the heatsink is immersed in oil and cooled to the oil's temperature.
5) In the $R_{dson}(T_j)$ calculation module, with I_{MOT} and V_{BAT} being sensed for motor control, the P_{loss} of the

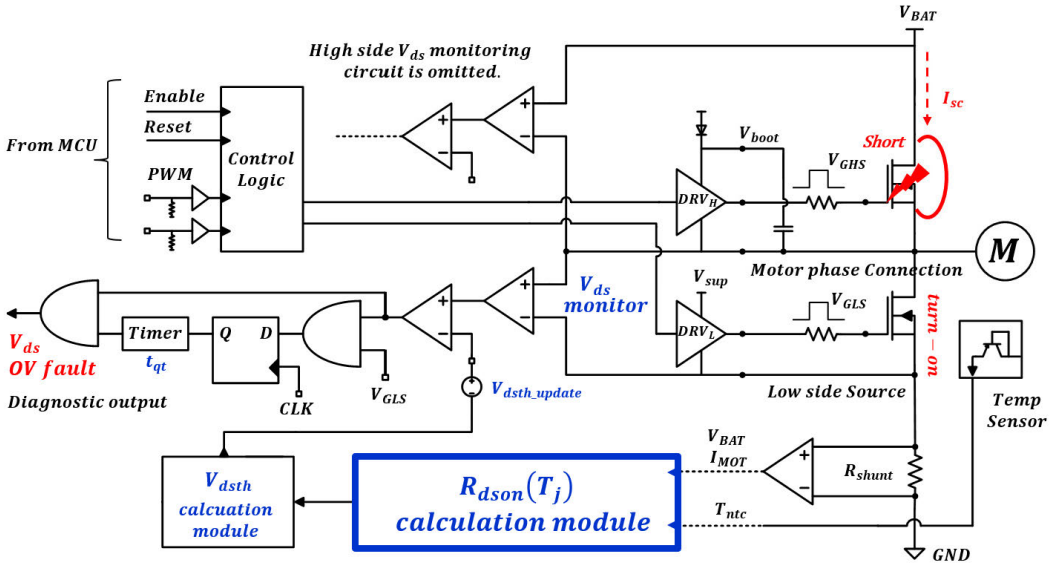

FIGURE 8. System architecture of the proposed online SC protection method with programmable V_{dsth}.

current one-cycle and ΔT_{j-ntc} are mapped from the $P_{loss} - \Delta T_{j-ntc}$ transfer table. Then, T_j can be calculated by adding the current T_{ntc}, and $R_{dson}(T_j)$ can be also obtained.

6) Based on the previously estimated T_j, V_{dsth_update} can be calculated by an integer multiple of the corresponding temperature range. Then, the new V_{dsth_update} is updated in the register.
7) If an SC event does not occur, the V_{dsth} will be updated according to T_j or the last value of V_{dsth} will be maintained according to the presence or absence of the change in the T_{ntc} section. If an SC event occurs, the V_{ds} OV fault is triggered and, after 1.4 μs, the affected MOSFET is turned off and the SCC is cut off.

The system architecture of the SC protection method is described in Fig. 8. The SCB event case was also considered. The SCG event case can be considered the same as the SCB one. If the high-side MOSFET was shortened in one leg of the inverter and the low-side MOSFET was switched on, it detects that the voltage between the motor phase connection and source pin of the low-side MOSFET is greater than the pre-set V_{dsth} through the voltage follower and the comparator circuit. The output of the comparator passes through the timer circuits and, after t_{qt}, the V_{ds} OV fault signal is generated and the gate drive lowers the affected MOSFET. The timer circuits are composed of a debouncing circuit and a time delay circuit for t_{qt}. The debouncing circuit causes the timer to start whenever the comparator output indicates a V_{ds} OV fault and resets the timer whenever the comparator output returns to normal. In the time delay circuit, the V_{ds} OV fault flag and fault bit are only activated when the fault state is maintained over the qualification time t_{qt}.

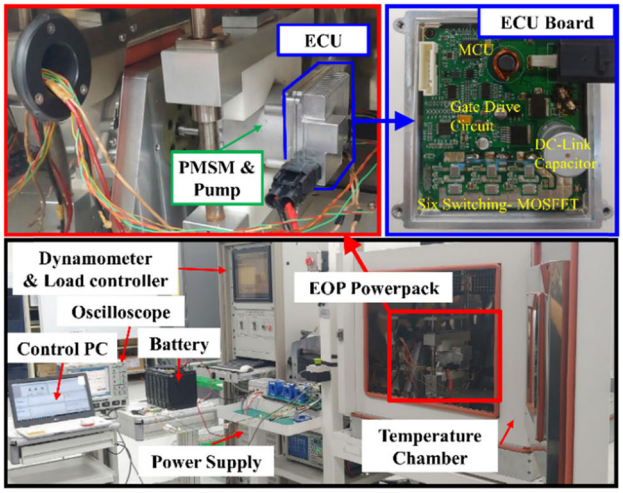

FIGURE 9. Prototype of the EOP powerpack and test bench set up.

V. EXPERIMENTAL VERIFICATION

A. PROTOTYPE OF THE EOP POWERPACK AND TEST BENCH

The EOP powerpack prototype was fabricated as shown in Fig. 9. It was a powerpack type in which the pump, motor and ECU were integrated and assembled. The diameter and length of the power pack was 86 mm and 134 mm, the rated power was 192 W. The pump was an interior gear type and the motor type was surface-mounted permanent magnet synchronous motor with a 6-pole and 9-slot combination. The ECU was designed on one board (FR4 with six-layers) with an external 13.5-V supply voltage line and CAN communication line.

TABLE 6. The comparison of the estimation and measurement results.

T_{amb} (°C)	Estimation $R_{dson}(T_j)$ (mΩ)	Estimation (V_{dsth}= 500 mV)		Measurement (V_{dsth}= 500 mV)		Difference between estimation and measurement			
		I_{det} [A]	I_{pk} [A]	I_{DET} [A]	I_{PK} [A]	I_{det} - I_{DET}		I_{pk} - I_{PK}	
						[A]	[%] [a]	[A]	[%] [a]
25	1.954	221.8	278.9	220.5	277.3	1.3	0.6	1.6	0.6
70	2.295	192.7	253.2	190.4	251.5	2.3	1.2	1.7	0.7
105	2.602	172.3	235.3	167.9	231.2	4.4	2.6	4.1	1.8
130	2.854	158.5	223.2	149.3	214.1	9.2	6.2	9.1	4.3

[a][%] means; tolerance rate = $\frac{(I_{det}-I_{DET})}{I_{DET}} \times 100$ or $\frac{(I_{pk}-I_{PK})}{I_{PK}} \times 100$

The test bench consisted of an automotive battery with a power supply connected in parallel, as well as a dynamometer, oscilloscope, load controller, a control PC and EOP powerpack within a controllable temperature chamber. In a real vehicle environment, the EOP would be immersed in ATF oil. However, the oil temperature around the EOP was replaced by setting the ambient temperature of the controllable temperature chamber due to the difficulty of setting up the oil circulation equipment. For the SC test, the jumper wire and switch for the SC event were connected to the drain and source pins of one high-side MOSFET of the three legs of the inverter. When the switch for SCB was closed while the motor was running, an SCB event occurred and the SCC was measured by applying a current probe to the jumper wire connected to the high-side MOSFET. Moreover, the bridge voltage V_{BAT} point connected to the drain of the high-side MOSFET and V_{gs} of the low-side MOSFET were measured simultaneously. After the powerpack in the ECU's off state had been saturated at 25°C, 70°C, 105°C and 130°C of the chamber temperature T_{amb} (with the condition that the T_{ntc} was the same as the T_{amb}), the ECU was turned on and operated under continuous operation conditions. The continuous load profile was 3.1 LPM @ 4.0 Bar in terms of the hydraulic pressure and flow rate of the pump, and the required motor torque and speed was 0.135 Nm and 3000 rpm, respectively, and the continuous phase current was 10 A. When the T_{ntc} was saturated by continuously operating the powerpack, the SCB event was produced and the I_{sc}, V_{BAT} and V_{gs} were measured.

B. VERIFICATION OF THE SCC MAP AND $R_{dson}(T_j)$ CALCULATION MODULE

The comparative experiment was conducted to verify the accuracy of the SCC map and the $R_{dson}(T_j)$ calculation module. In this case, the online SC protection method was not applied. That is, after fixing V_{dsth} to 500 mV without changing the V_{dsth} value, the SCCs were measured at T_{amb} of 25°C, 70°C, 105°C and 130°C, respectively. The measured I_{DET} and I_{PK} were compared with the predicted I_{det} and I_{pk}. In Table 6, the estimated values of $R_{dson}(T_j)$, I_{det}, and I_{pk} in each T_{amb} were calculated from $R_{dson}(T_j)$ calculation module during motor running and stored in the MCU's memory. In I_{DET} and I_{PK}, the uppercase letters of the subscript refer to the measured values. Moreover, the measured I_{DET} and I_{PK} values came from the measured graphs of the SCCs as shown in Fig. 10(a)–(d). On the basis of the results in Table 6, the I_{DET} values were measured as 1.3 A to 9.2 A smaller than the estimated I_{det} values, and the I_{PK} values were measured as 1.6 A to 9.1 A smaller than the estimated I_{pk} values. Therefore, compared to the estimated values, the measured I_{DET} had a deviation of 0.6%–6.2% and the measured I_{PK} of 0.6%–4.3%. As the T_{amb} increased, the deviation tended to gradually become worse, and it was expected that there was main reason for the difference between the estimated and measured values.

In the SCC map, additional parasitic resistance values such as the contact resistance and PCB pattern resistance were assumed to be 0.3 mΩ regardless of the PCB temperature. In reality, however, the 0.3 mΩ was an appropriate value at RT, but as the ambient temperature increased, so too did the parasitic resistance and so it could be increased to 0.5 mΩ at T_{amb} 130°C. Considering the parasitic resistance value of 0.5 mΩ instead of 0.3 mΩ at the T_{amb} of 130°C, I_{det} value is calculated as 149.1 A and so the I_{DET} value would have a difference of less than 1 A, rather than 9.2 A, as compared to the estimated I_{det}.

In summary, even if there was a difference in the hot temperature, the accuracy of the SCC map and the $R_{dson}(T_j)$ calculation module were valid because the tendency of the estimated I_{det} and I_{pk}, according to the temperature, was very similar to the measured values and the difference was also small compared to the magnitude of the SCCs. If the parasitic resistances are calibrated with the experimental data, a more accurate SCC map can be expected. At each T_{amb}, the SCCs had a triangular wave shape that was very similar to that of the estimated SCCW graph, as shown in the measured graph in Fig. 10(a)–(d). As can be seen from the measured SCCW, the entire period from the occurrence of the SCB to the gate drive output low is extremely short, i.e., 5 μs or less. At the point of I_{PK}, the V_{gs} of the low-side MOSFET dropped rapidly and became low and the V_{BAT} also dropped instantaneously.

C. VERIFICATION OF THE ONLINE SC PROTECTION METHOD

To verify the proposed online SC protection method with the automatic programmable fault threshold, the SC events were

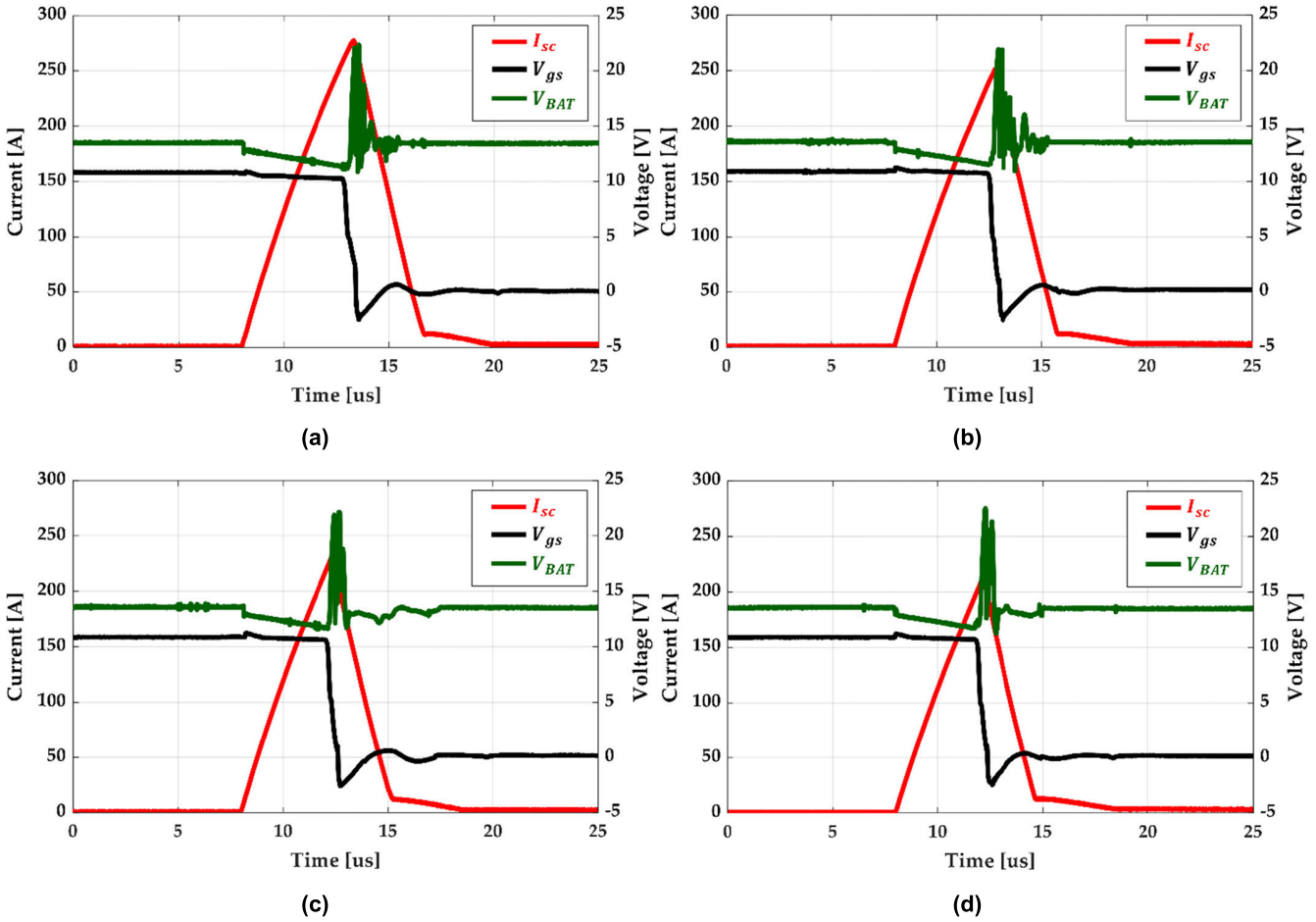

FIGURE 10. Measured waveforms of the I_{sc}, V_{gs} of the low-side MOSFET, and V_{BAT}: (a) when T_{amb} = 25°C, I_{DET} = 220.5 A and I_{PK} = 277.3 A, (b) when T_{amb} = 70°C, I_{DET} = 190.4 A and I_{PK} = 251.5 A, (c) when T_{amb} = 105°C, I_{DET} = 167.9 A and I_{PK} = 231.2 A, (d) when T_{amb} = 130°C, I_{DET} = 149.3 A and I_{PK} = 214.1 A.

TABLE 7. Comparison of the estimation and measurement results.

T_{amb} (°C)	V_{dsth} (mV)	Estimation		Measurement		Difference between estimation and measurement			
						I_{det} - I_{DET}		I_{pk} - I_{PK}	
		I_{det} [A]	I_{pk} [A]	I_{DET} [A]	I_{PK} [A]	[A]	[%] [a]	[A]	[%] [a]
25	350	155.3	220.5	153.6	219.2	1.7	1.1	1.3	0.6
70	400	154.2	219.5	152.2	218.0	2.0	1.3	1.5	0.7
105	450	155.1	220.4	151.5	217.3	3.6	2.4	3.1	1.4
130	500	158.3	222.9	148.7	213.8	9.6	6.5	9.1	4.3

[a][%] means; tolerance rate = $\frac{(I_{det}-I_{DET})}{I_{DET}} \times 100$ or $\frac{(I_{pk}-I_{PK})}{I_{PK}} \times 100$

tested at T_{amb} of 25°C, 70°C, 105°C and 130°C. The V_{dsth} values were changed through the proposed protection method and the measured I_{DET} and I_{PK} values at each T_{amb} are described in Table 7. Considering the measurement results, the measured I_{DET} values were measured at 1.7 A–9.6 A smaller than the estimated values, and the measured I_{PK} values were measured 1.3 A–9.1 A smaller than the estimated ones. The reason for the difference was deviations from the parasitic resistance values at hot temperature, as described above. Compared to the estimated values, the measured I_{DET} featured a deviation of 1.1%–6.5% and the measured I_{PK} had a deviation of 0.6%–4.3%. As the T_{amb} increased, the deviation also tended to gradually become worse. Although the measured I_{DET} and I_{PK} values had a few amperes of difference from the estimated values, it could be confirmed that the SCC can be controlled. The I_{DET} and I_{PK} values were

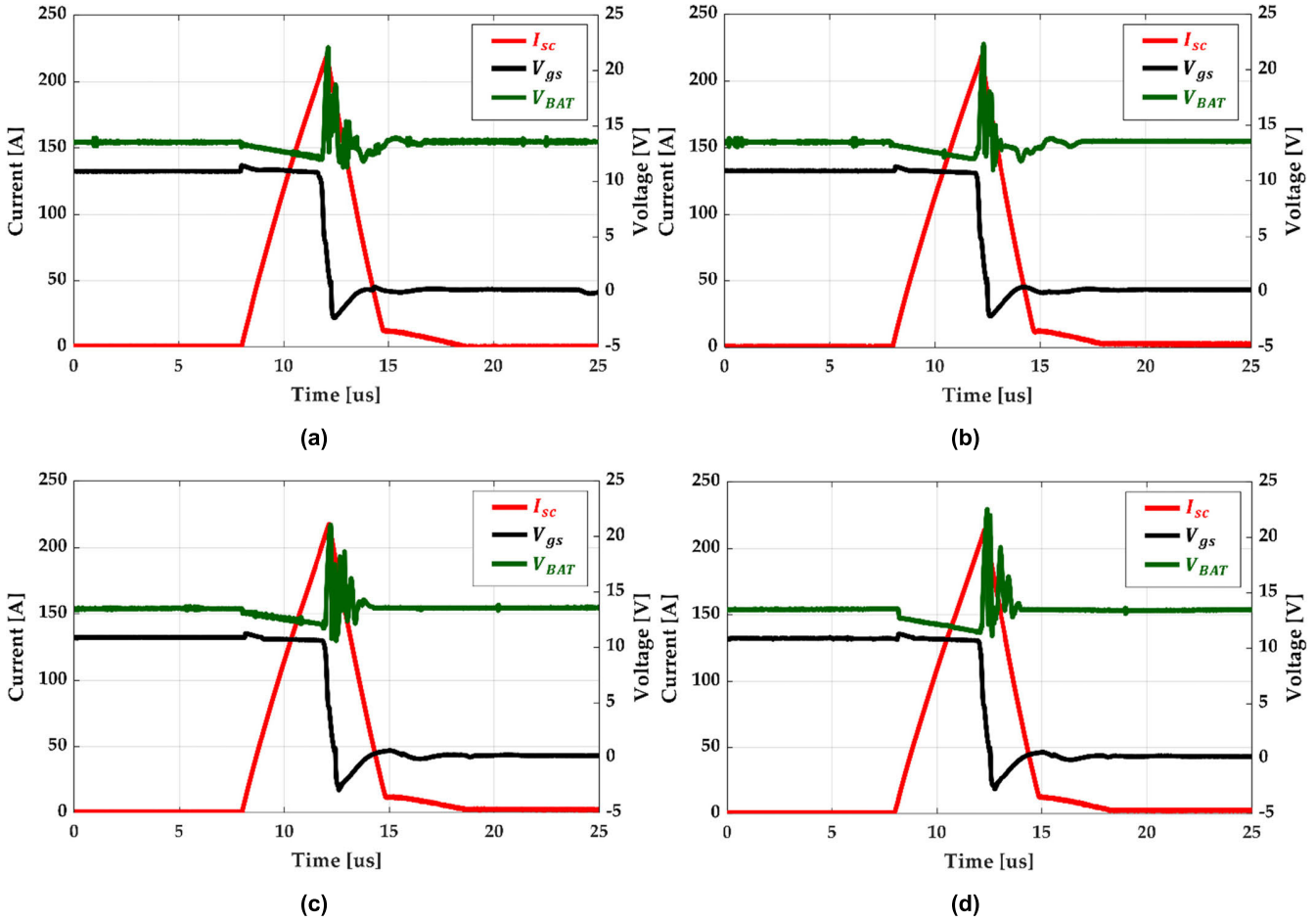

FIGURE 11. Measured waveforms of the I_{sc}, V_{gs} of the low-side MOSFET, and V_{BAT}: (a) when T_{amb} = 25°C, I_{DET} = 153.6 A and I_{PK} = 219.2 A, (b) T_{amb} = 70°C, I_{DET} = 152.2 A and I_{PK} = 218 A, (c) when T_{amb} = 105°C, I_{DET} = 151.5 A and I_{PK} = 217.3 A and (d) when T_{amb} = 130°C, I_{DET} = 148.7 A and I_{PK} = 213.8 A.

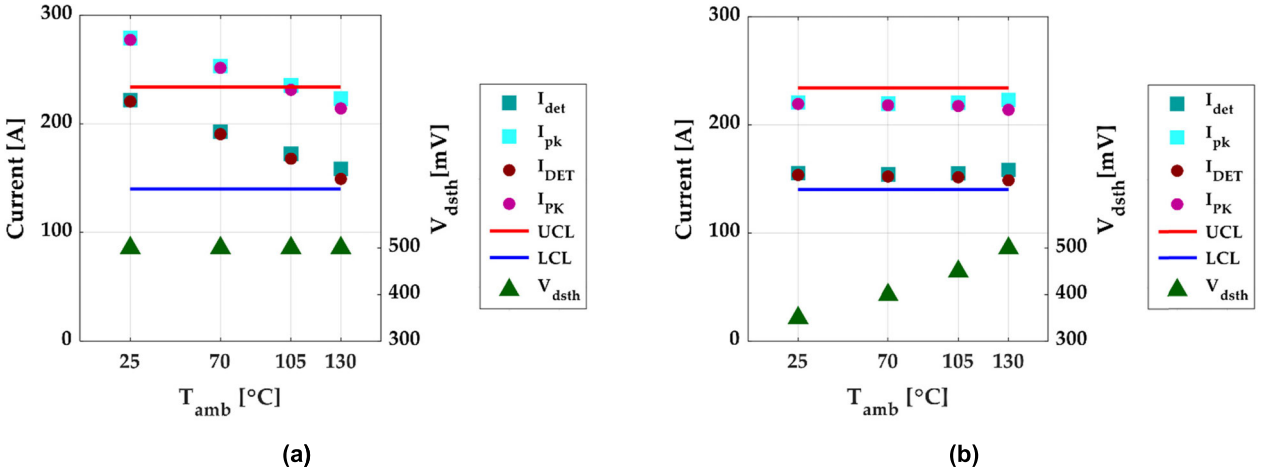

FIGURE 12. Comparison of the SCCs measurement results: (a) when V_{dsth}(= 500 mV) was fixed and (b) when V_{dsth} was changed by 350, 400, 450 and 500 mV.

similarly measured according to the variable V_{dsth}, regardless of T_{amb}. And, Fig. 11(a)–(d) shows the SCC, V_{gs} and V_{BAT} waveforms measured at each T_{amb}.

Fig. 12(a) and (b) show the deviations in the I_{DET} and I_{PK} values at each T_{amb} when V_{dsth} is fixed and variable. When the V_{dsth} value was fixed to 500 mV, the difference

was 71.2 A for I_{DET} and 63.2 A for I_{PK} depending on the temperature. However, when the V_{dsth} values were varied, the difference decreased to 4.9 A for I_{DET} and 5.4 A for I_{PK}. Based on the maximum value of I_{DET}, the deviation in the I_{DET} according to the temperature was reduced from 32.3% to 3.2% and based on the maximum value of I_{PK}, the deviation in the I_{PK} according to temperature was reduced from 22.8% to 2.5% via the online SC protection method. As shown in Fig. 12(a) and (b), V_{dsth} according to four temperature ranges is variable and set again, so that I_{DET} and I_{PK} values are distributed between the UCL and LCL.

VI. CONCLUSION

Herein, an online SC protection method with an automatic fault threshold was proposed to detect SC failures in an automotive EOP powerpack exposed to operating environments with diverse ambient operating temperatures and to various load conditions. The key-features to be addressed in this study can be summarised as follows.

1) In the V_{ds} monitoring protection method, a system with a fixed fault threshold cannot control the SCC within the defined protection range because the SCC fluctuation according to $R_{dson}(T_j)$ variation. This can lead to failures in protection or diagnosis. To solve this problem, the proposed method monitors the change of $R_{dson}(T_j)$ and applies differently to the optimal fault threshold according to $R_{dson}(T_j)$, reducing the SCC fluctuation and controlling the SCC within protection range.
2) The numerical approach method through worst-case conditions for the protection range setting and qualification time setting, which are the prerequisites for the optimal fault threshold selection, was presented. In particular, it was emphasised that the qualification time must be carefully selected in consideration of the trade-off relationship between V_{gs} and V_{ds} monitoring of the automotive 3-Phase low-voltage MOSFET driver circuit.
3) The biggest drawback of the V_{ds} monitoring protection method by voltage sensing, not current, was that accurate SCC cannot be predicted. However, through circuit analysis and simulation, SCCW was estimated and the key factors of the SCC represented by I_{det} and I_{pk} were predicted. To control I_{det} and I_{pk}, the $R_{dson}(T_j)$, which changes owing to the operating temperature and load of the EOP powerpack, must be estimated. To make this possible, the $R_{dson}(T_j)$ calculation module is developed with simulation and experimental data.

The methods proposed herein was verified on the basis of circuit analysis, simulation results and experimental results. In addition, the verified SC protection method aim to universally applicable to automotive low-voltage gate drive circuit and logic design. The new protection method can improve the quality of diagnosis to higher levels and will establish itself as a powerful mechanism for ensuring functional safety. As future research, with the commercialisation of an autonomous vehicles, more research is needed on a protection method that enables not only the fault detection but also the healing of the failures.

REFERENCES

[1] Y. Kim, J. Lee, C. Jo, Y. Kim, M. Song, J. Kim, and H. Kim, "Development and control of an electric oil pump for automatic transmission-based hybrid electric vehicle," *IEEE Trans. Veh. Technol.*, vol. 60, no. 5, pp. 1981–1990, Jun. 2011.
[2] Y. Liu, Y. Zhou, J. Wang, D. Qu, and F. Zhang, "Hydraulic system control for a hybrid continuously variable transmission based on an electric oil pump," *IEEE Trans. Veh. Technol.*, vol. 67, no. 11, pp. 10398–10410, Nov. 2018.
[3] Y. Liu, X. Wu, H. Li, S. Wei, J. Gu, and B. Wen, "Simulation and intelligent cooperation control strategy of double-pump hydraulic system for automatic transmissions," in *Proc. 12th Int. Conf. Intell. Syst. Knowl. Eng. (ISKE)*, Nanjing, China, Nov. 2017, pp. 1–6.
[4] J. Wi, H. Kim, J. Yoo, H. Son, H. Kim, and B. Kim, "Energy consumption of parallel type hybrid electric vehicle with continuously variable transmission using electric oil pump," in *Proc. 13th Int. Conf. Ecol. Vehicles Renew. Energies (EVER)*, Monte-Carlo, Monaco, Apr. 2018, pp. 1–7.
[5] K.-Y. Yoon and S.-W. Baek, "Robust design optimization with penalty function for electric oil pumps with BLDC motors," *Energies*, vol. 12, no. 1, p. 153, Jan. 2019.
[6] H. Kim, J. Wi, J. Yoo, H. Son, C. Park, and H. Kim, "A study on the fuel economy potential of parallel and power split type hybrid electric vehicles," *Energies*, vol. 11, no. 8, p. 2103, Aug. 2018.
[7] A. Fauda, L. Marchetti, F. Cola lng, and L. Arena lng, "Innovative electric oil pumps for different automotive applications," SAE Tech. Paper 2020-24-0022, Sep. 2020.
[8] Bosch. (2019). *Electric Oil Pump for Transmission*. [Online]. Available: https://www.bosch.co.jp/aee2019/pdf/bosch-automotive-engineering-exposition-2019-electrified–electric-oil-pump-for-transmission-en-01.pdf
[9] P. D. Reigosa, F. Iannuzzo, H. Luo, and F. Blaabjerg, "A short-circuit safe operation area identification criterion for SiC MOSFET power modules," *IEEE Trans. Ind. Appl.*, vol. 53, no. 3, pp. 2880–2887, May 2017.
[10] A. Fayyaz, L. Yang, and A. Castellazzi, "Transient robustness testing of silicon carbide (SiC) power MOSFETs," in *Proc. 15th Eur. Conf. Power Electron. Appl. (EPE)*, Lille, France, Sep. 2013, pp. 1–10.
[11] Z. Wang, X. Shi, L. M. Tolbert, F. Wang, Z. Liang, D. Costinett, and B. J. Blalock, "Temperature-dependent short-circuit capability of silicon carbide power MOSFETs," *IEEE Trans. Power Electron.*, vol. 31, no. 2, pp. 1555–1566, Feb. 2016.
[12] D.-P. Sadik, J. Colmenares, D. Peftitsis, G. Tolstoy, J. Rabkowski, and H.-P. Nee, "Analysis of short-circuit conditions for silicon carbide power transistors and suggestions for protection," in *Proc. 16th Eur. Conf. Power Electron. Appl.*, Lappeenranta, Finland, Aug. 2014, pp. 1–10.
[13] N. Badawi, A. E. Awwad, and S. Dieckerhoff, "Robustness in short-circuit mode: Benchmarking of 600 V GaN HEMTs with power Si and SiC MOSFETs," in *Proc. IEEE Energy Convers. Congr. Exposit. (ECCE)*, Milwaukee, WI, USA, Sep. 2016, pp. 1–7.
[14] B. Lu and S. K. Sharma, "A literature review of IGBT fault diagnostic and protection methods for power inverters," *IEEE Trans. Ind. Appl.*, vol. 45, no. 5, pp. 1770–1777, Jul. 2009.
[15] J.-H. Choi, K. Jin-Hong, J. Sung Park, B.-G. Gu, and C.-Y. Won, "A new short circuit protection scheme for small inverters," in *Proc. IEEE Vehicle Power Propuls. Conf.*, Seoul, South Korea, Oct. 2012, pp. 1544–1547.
[16] A. Radun, "An alternative low-cost current-sensing scheme for high-current power electronics circuits," *IEEE Trans. Ind. Electron.*, vol. 42, no. 1, pp. 78–84, Feb. 1995.
[17] M. Oinonen, M. Laitinen, and J. Kyyra, "Current measurement and short-circuit protection of an IGBT based on module parasitics," in *Proc. 16th Eur. Conf. Power Electron. Appl.*, Lappeenranta, Finland, Aug. 2014, pp. 1–9.
[18] J. Wang, Z. Shen, C. DiMarino, R. Burgos, and D. Boroyevich, "Gate driver design for 1.7 kV SiC MOSFET module with Rogowski current sensor for shortcircuit protection," in *Proc. IEEE Appl. Power Electron. Conf. Expo. (APEC)*, Long Beach, CA, USA, Mar. 2016, pp. 516–523.
[19] Y. Sukhatme, M. V. Krishna, P. Ganesan, and K. Hatua, "A drain current based short circuit protection technique for SiC MOSFET," in *Proc. Int. Symp. Devices, Circuits Syst. (ISDCS)*, Howrah, India, Mar. 2018, pp. 1–6.

[20] Z. Wang, X. Shi, Y. Xue, L. M. Tolbert, F. Wang, and B. J. Blalock, "Design and performance evaluation of overcurrent protection schemes for silicon carbide (SiC) power MOSFETs," *IEEE Trans. Ind. Electron.*, vol. 61, no. 10, pp. 5570–5581, Oct. 2014.

[21] L. Pierre, B. Dominique, M. Herve, A. Bruno, and R. Jean-Francois, "Fast over-current protection of high power IGBT modules," in *Proc. Eur. Conf. Power Electron. Appl.*, Dresden, Germany, Sep;. 2005, pp. 1–10.

[22] J. Wang, Z. Shen, R. Burgos, and D. Boroyevich, "Integrated switch current sensor for shortcircuit protection and current control of 1.7-kV SiC MOSFET modules," in *Proc. IEEE Energy Convers. Congr. Expo. (ECCE)*, Milwaukee, WI, USA, Sep. 2016, pp. 1–7.

[23] T. Horiguchi, S. Kinouchi, Y. Nakayama, and H. Akagi, "A fast short-circuit protection method using gate charge characteristics of SiC MOSFETs," in *Proc. IEEE Energ. Conv. Cong. Expo. (ECCE)*, Montreal, QC, Canada, Oct. 2015, pp. 4759–4764.

[24] Y. Cui, Z. Zhang, P. Yi, and L. Wei, "Investigation of current mirror based overcurrent protection for 1200 V 800 A high power SiC MOSFET modules," in *Proc. IEEE Energy Convers. Congr. Expo. (ECCE)*, Baltimore, MD, USA, Sep. 2019, pp. 6161–6165.

[25] A. Niwa, T. Imazawa, R. Kojima, M. Yamamoto, T. Sasaya, T. Isobe, and H. Tadano, "A dead-time-controlled gate driver using current-sense FET integrated in SiC MOSFET," *IEEE Trans. Power Electron.*, vol. 33, no. 4, pp. 3258–3267, Apr. 2018.

[26] Y. Shi, R. Xie, L. Wang, Y. Shi, and H. Li, "Short-circuit protection of 1200 V SiC MOSFET T-type module in PV inverter application," in *Proc. IEEE Energy Convers. Congr. Expo. (ECCE)*, Milwaukee, WI, USA, Sep. 2016, pp. 1–5.

[27] D.-P. Sadik, J. Colmenares, G. Tolstoy, D. Peftitsis, M. Bakowski, J. Rabkowski, and H.-P. Nee, "Short-circuit protection circuits for silicon-carbide power transistors," *IEEE Trans. Ind. Electron.*, vol. 63, no. 4, pp. 1995–2004, Apr. 2016.

[28] T. Bertelshofer, A. Maerz, and M. Bakran, "Design rules to adapt the desaturation detection for SiC MOSFET modules," in *Proc. PCIM Euro. Int. Exhib. Conf. Power Electron., Intel. Motion, Renew. Energ. Energ. Manage.*, Nuremberg, Germany, May 2017, pp. 1–8.

[29] J. Kim and Y. Cho, "Overcurrent and short-circuit protection method using desaturation detection of SiC MOSFET," in *Proc. IEEE PELS Workshop Emerg. Technol., Wireless Power Transf. (WoW)*, Seoul, South Korea, Nov. 2020, pp. 197–200.

[30] A. E. Awwad and S. Dieckerhoff, "Short-circuit evaluation and overcurrent protection for SiC power MOSFETs," in *Proc. 17th Eur. Conf. Power Electron. Appl. (EPE ECCE-Europe)*, Geneva, Switzerland, Sep. 2015, pp. 1–9.

[31] J. Rice and J. Mookken, "SiC MOSFET gate drive design considerations," in *Proc. IEEE Int. Workshop Integr. Power Packag. (IWIPP)*, Chicago, IL, USA, May 2015, pp. 24–27.

[32] P. Hofstetter and M.-M. Bakran, "The two-dimensional short-circuit detection protection for SiC MOSFETs in urban rail transit application," *IEEE Trans. Power Electron.*, vol. 35, no. 6, pp. 5692–5701, Jun. 2020.

[33] P. Hofstetter, S. Hain, and M. Bakran, "Applying the 2D-short circuit detection method to SiC MOSFETs including an advanced soft turn off," in *Proc. PCIM Euro. Int. Exhib. Conf. Power Electron., Intel. Motion, Renew. Energ. Energ. Manage.*, Nuremberg, Germany, 2018, pp. 1–7.

[34] R. Wang, Q. Sun, W. Hu, Y. Li, D. Ma, and P. Wang, "SoC-based droop coefficients stability region analysis of the battery for stand-alone supply systems with constant power loads," *IEEE Trans. Power Electron.*, vol. 36, no. 7, pp. 7866–7879, Jul. 2021, doi: 10.1109/TPEL.2021.3049241.

[35] S. Srinivasan, J. S. Kumar, K. Vijayakumar, P. Venkataraman, and S. Loganathan, "Performance improvement of automotive oil pump to operate at high temperatures employed in modern diesel engine," SAE Tech. Paper 2012-01-0428, Apr. 2012.

[36] Infineon. (2014). *AUIRF8736M2TR Datasheet*. [Online]. Available: https://www.infineon.com/dgdl/auirf8736m2.pdf?fileId=5546d462533600a4015355b0dade1414

[37] R. Murphree, S. Roy, A. Abbasi, P. Assem, R. C. N. Pilawa-Podgurski, and A. Mantooth, "A flip-chip capable low-side and high-side SOI gate driver with variable drive strength for GaN power FETs," in *Proc. IEEE 7th Workshop Wide Bandgap Power Devices Appl. (WiPDA)*, Raleigh, NC, USA, Oct. 2019, pp. 113–120.

[38] S. Weber, A. Merkert, and A. Mertens, "Gate driver for safe operation of depletion mode SiC JFETs," in *Proc. IEEE Energy Convers. Congr. Expo. (ECCE)*, Pittsburgh, PA, USA, Sep. 2014, pp. 5716–5722.

[39] Allegro Microsystems. (2016). *A4911KJPTR-T Datasheet*. [Online]. Available: https://www.allegromicro.com/en/products/motor-drivers/bldc-drivers/a4911

[40] Vishay. (2016). *Power MOSFET Basics: Understanding Gate Charge and Using it to Assess Switching Performance*. [Online]. Available: https://www.vishay.com/docs/73217/an608a.pdf

[41] A. Huang. (2012). *OptiMOSTM Power MOSFET Datasheet Explanation*. Infineon Technologies AG. [Online]. Available: https://www.infineon.com/dgdl/Infineon-MOSFET_OptiMOS_datasheet_explanation-AN-v01_00-EN.pdf?fileId=db3a30433b47825b013b6b8c6a3424c4

[42] Infineon Technologies AG. (2020). *Transient Thermal Measurements and Thermal Equivalent Circuit Models*. [Online]. Available: https://www.infineon.com/dgdl/Infineon-Thermal_equivalent_circuit_models-ApplicationNotes-v01_02-EN.pdf?fileId=db3a30431a5c32f2011aa65358394dd2

[43] K. Yang, J. Guo, H. Ge, B. Bilgin, V. Loukanov, and A. Emadi, "Transient electro-thermal analysis for a MOSFET based traction inverter," in *Proc. IEEE Transp. Electrific. Conf. Expo (ITEC)*, Dearborn, MI, USA, Jun. 2014, pp. 1–6.

[44] M. H. M. Sathik, T. K. Jet, K. Kandasamy, S. Prasanth, R. Simanjorang, A. K. Gupta, and G. Chandana, "Online electro-thermal model for real time junction temperature estimation for insulated gate bipolar transistor (IGBT)," in *Proc. IEEE 2nd Annu. Southern Power Electron. Conf. (SPEC)*, Auckland, New Zealand, Dec. 2016, pp. 1–6.

[45] On Semiconductor. (2014). *MOSFET Transient Junction Temperature Under Repetitive Uis/Short-Circuit Conditions*. [Online]. Available: https://www.onsemi.com/pub/Collateral/AND9042-D.PDF

YOUNGWOO NOH (Graduate Student Member, IEEE) received the M.S. degree in electrical and computer engineering from Seoul National University, Seoul, South Korea, in 2005. He is currently pursuing the Ph.D. degree with the Department of Electrical Engineering, Hanyang University, Seoul. Since 2005, he has been researching on automotive motor drive engineering and is currently working as a Professional Engineer with the LG IT Research and Development Center. His research interests include electric motor control, power electronics, automotive electronic controller design, fault-tolerant design, functional safety design, and hybrid electric vehicles.

WONKYU KIM received the M.S. degree in electrical engineering from Hanbat University, Deajeon, South Korea, in 2011. He is currently pursuing the Ph.D. degree with the Department of Electrical Engineering, Hanyang University, Seoul, South Korea. Since 2011, he has been researching on automotive motor drive engineering and is currently working as a Senior Engineer with the LG IT Research and Development Center. His research interests include electric motor control, power electronics, automotive electronic controller design, automotive sensor design, and hybrid electric vehicles.

JU LEE (Senior Member, IEEE) received the M.S. degree from Hanyang University, Seoul, South Korea, in 1988, and the Ph.D. degree in electrical engineering from Kyusyu University, Japan, in 1997. He joined Hanyang University, in 1997, where he is currently a Professor with the Department of Electrical and Bio-Engineering. His main research interests include electric machinery and its drives, electro-magnetic field analysis, transportation systems, such as hybrid electric vehicles and railway propulsion systems. He is a member of the IEEE Industry Applications Society, the Magnetics Society, and the Power Electronics Society.